IEEE Access
Multidisciplinary ⋮ Rapid Review ⋮ Open Access Journal

Received 26 January 2023, accepted 15 March 2023, date of publication 31 March 2023, date of current version 13 April 2023.

Digital Object Identifier 10.1109/ACCESS.2023.3263555

RESEARCH ARTICLE

Comprehensive Analysis of Wireless Capsule Endoscopy Radio Channel Characteristics Using Anatomically Realistic Gastrointestinal Simulation Model

MARIELLA SÄRESTÖNIEMI[1,2], (Senior Member, IEEE), ATTAPHONGSE TAPARUGSSANAGORN[3,4], JUTHATIP WISANMONGKOL[3,4], MATTI HÄMÄLÄINEN[2], (Senior Member, IEEE), AND JARI IINATTI[2], (Senior Member, IEEE)

[1]Faculty of Medicine, Research Unit of Health Sciences and Technology, University of Oulu, 90014 Oulu, Finland
[2]Centre for Wireless Communications, Faculty of Information Technology and Electrical Engineering, University of Oulu, 90014 Oulu, Finland
[3]Telecommunications Academic Program, ICT Department, Asian Institute of Technology, Khlong Nueng 12120, Thailand
[4]School of Engineering and Technology, Asian Institute of Technology, Khlong Nueng 12120, Thailand

Corresponding author: Mariella Särestöniemi (mariella.sarestoniemi@oulu.fi)

This work was supported in part by the Academy of Finland Profi6 Funding, 6G Enabling Sustainable Society (University of Oulu), the Academy of Finland 6G Flagship, under Grant 318927; and in part by the European Union's Horizon 2020 Programme under the Marie Sklodowska-Curie under Grant 872752.

ABSTRACT This paper presents a comprehensive study of radio channels related to capsule endoscopy communications in ultra wideband wireless body area networks (UWB-WBAN) utilizing multiple antenna systems. The research includes 363 channel realizations, obtained through simulations using an anatomically realistic human voxel model and a capsule model. A capsule position is modelled in such a way that it moves throughout the entire intestinal tract. The study examines the frequency and time domain characteristics of the channels in various capsule locations, including the most challenging positions deep inside the tissues or far away from most of the antennas. Additionally, the propagation characteristics inside the abdominal tissue are studied by calculating the most obvious propagation paths based on power flow illustrations and reflecting the results with the channel impulse response analysis. The impact of capsule rotation is also studied. It is shown how small changes in capsule location can greatly impact on the channel characteristics if the thickness of the tissues between the capsule and the on-body antenna changes significantly. The paper concludes with statistical analysis of the channel data, including path loss and root mean square (RMS) delay spread. The results provide valuable insight into how the signal propagates inside different parts of the gastrointestinal tract. They show that channel attenuation remains moderate along most of the gastrointestinal tract, and that even the deepest locations in the small intestine area can be resolved with the use of directional on-body antennas and receivers with higher sensitivity.

INDEX TERMS Channel modeling, implant communications, in-body propagation, path loss, power flow analysis, realistic voxel models, RMS delay spread.

I. INTRODUCTION

Wireless Capsule Endoscopy (WCE) is a reliable and painless method for investigating abnormalities in the gastrointestinal tract. It can detect tumors, polyps, Crohn's disease, and bleeding. However, one of the challenges of using WCE to investigate the entire intestinal tract is the duration of the capsule's battery, particularly for people with slower digestive systems. To address this challenge, capsules are activated after a certain amount of time after swallowing, depending on whether the goal is to investigate the small intestine or colon [1], [2], [3], [4], [5], [6], [7], [8].

The associate editor coordinating the review of this manuscript and approving it for publication was Parul Garg.

Already a decade ago, researchers have recognized that ultra wideband (UWB) technology could provide several advantages for WCE, such as high-resolution images and high data rates, while also being low-power and reliable [9]. Since then, propagation in the context of UWB capsule endoscopy has been studied actively [10], [11], [12], [13], [14], [15], [16], [17], [18], [19].

One of the main challenges related to UWB-based WCE is the high propagation loss in the tissues [19], [21], [22]. One approach to overcome this challenge is to use directional on-body antennas that focus the radiation towards the body, while still meeting the specific absorption ratio (SAR) criteria, and hence strengthening the communication link between the in-body and the on-body device [23], [24]. Since the human intestinal system is wide and complex, a multiantenna system is essential to obtain full coverage on the intestinal area especially at UWB frequencies between 3.1 – 10.6 GHz [25], [26]. Besides, the multiantenna system is essential for capsule localization [27].

This paper presents a comprehensive radio channel study for WCE in the UWB multiantenna system using an anatomically realistic human voxel simulation model. The comprehensive research includes 363 channel realizations which are obtained by moving the capsule model throughout the whole intestinal tract, including the stomach, small intestine, and colon areas. The research covers studies on the variation of the channel characteristics in different capsule locations, including the most challenging capsule locations deep inside the tissues or far away from most of the antennas, discussion on the number of on-body antennas and study on the impact of the capsule's rotation. Additionally, it is shown how even small changes in the capsule location may change the channel characteristics if the thickness of the tissues between the capsule and the on-body antenna changes significantly.

The novelty of this research is that, to the author's knowledge, other UWB capsule endoscope channel studies are not based on such comprehensive evaluations throughout the whole gastrointestinal tract using an anatomical voxel model and multiple directional on-body antennas. This paper evaluates a 7-antenna setup throughout the whole gastrointestinal tract, expanding on the previous results presented in [25] and [26] which only evaluated a few capsule locations with 5-antenna setup.

The paper is organized as follows: Section II presents the simulation scenario describing the on-body antenna, the capsule endoscope model, and the voxel model used in the simulations. Additionally, on-body antenna and capsule locations in the gastrointestinal tract are illustrated. Section IV provides good insight on the propagation inside the tissues by presenting power flow illustrations in different capsule locations. Section V presents both frequency and time domain channel evaluations in different capsule locations and reflect some example cases with propagation path calculations and power flow illustrations. Besides, the impact of the capsule rotation and impact of the capsule's small shifts are evaluated. Summary and conclusions are presented in Section VI.

II. SIMULATION SCENARIO

The study is carried out with Dassault Simulia CST Studio Suite [28] and its anatomical voxel model Laura. A simplified capsule model from the previous studies [25], [26] is used in the evaluations. Furthermore, a directional on-body antenna designed for low-band UWB in-body communications [24] is used. Details of the antennas, antenna locations and the voxel model are summarized in the following subsections.

A. ANTENNAS

1) ON-BODY ANTENNA

In this study, we use a directional on-body antenna designed for in-body communications in the low-band UWB frequency range of 3.75 - 4.25 GHz, in accordance with the IEEE 802.15.6 Wireless Body Area Networks (WBAN) standard [29]. The antenna's structure is illustrated in Fig. 1a. The antenna features a cavity (grey area in the antenna) to enhance its directivity towards the body. This antenna was originally introduced in [24] and has been used in several in-body channel studies in [18], [19], [25], and [26]. The realized gains of the antenna when located on the body are presented in Figs. 1b-d for frequencies 3.75 GHz, 4 GHz, and 4.25 GHz, which are the start, center, and end frequencies of the range of interest, respectively.

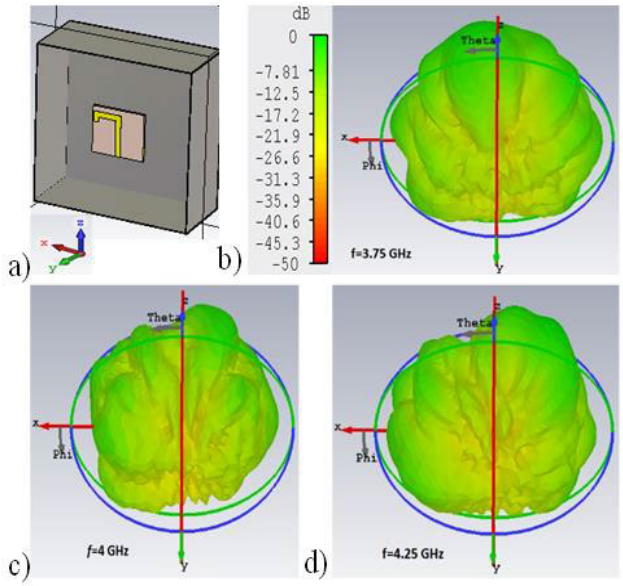

FIGURE 1. a) The directional cavity-backed on-body antenna designed for in-body communications, b) realized gain at 3.75 GHz, c) realized gain at 4 GHz, d) realized gain at 4.25 GHz.

2) CAPSULE ANTENNA

This study uses a simplified capsule model, in which an omnidirectional dipole antenna is embedded in a plastic capsule shell with realistic dimensions of 11 mm × 25 mm, similar to commercial capsules currently available [3]. The design of the dipole antenna and the capsule shell are presented in Fig. 3a-b, respectively. The dipole antenna is designed to

operate at the center frequency of 4 GHz inside the intestine. Additional information about capsule model can be found in [19]. The simulated reflection coefficients S11 for the on-body antenna and the capsule antenna are presented in Fig. 3. The S11 parameter for the on-body antenna is obtained in such a way that it is located on the voxel model's abdomen, with a 4 mm distance from the skin. This gap improves the antenna's radiation efficiency compared to the case the antenna is attached straight to the skin. The capsule antenna is placed inside the capsule model and set inside the voxel's small intestine, and its S11 parameter is simulated accordingly.

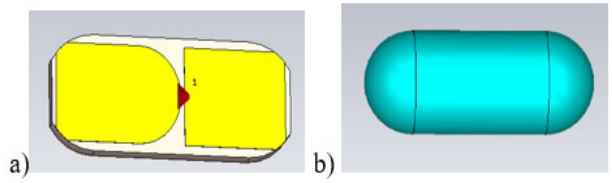

FIGURE 2. a) Dipole antenna inside the capsule model, b) the capsule shell with realistic capsule endoscope dimensions.

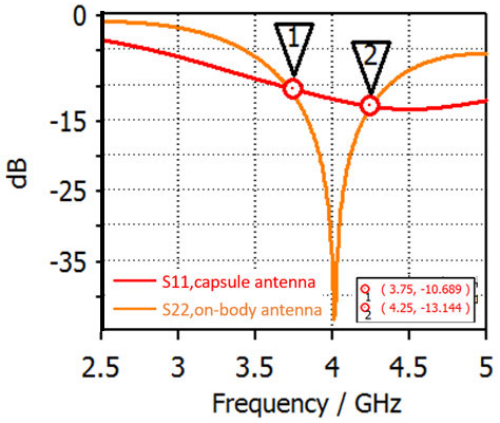

FIGURE 3. Antenna reflection coefficients for on-body antenna (as located on the voxel) and capsule antenna (as located inside the voxel's small intestine).

B. HUMAN VOXEL MODELS WITH ON-BODY ANTENNA LOCATIONS AND CAPSULE LOCATIONS

The study is carried out using Dassault Simulia CST Studio Suite [28], which is utilizing the finite integration technique (FIT). An anatomically realistic voxel model, Laura, illustrated in Fig. 4a, is used in the simulations to enable realistic radio channel evaluations between the capsule endoscope and the on-body antennas throughout the whole intestinal tract. Laura is designed to resemble a normal-weight woman, and the resolution of Laura-voxel at UWB frequencies is (1.88 × 1.88 × 1.25) mm.

1) ON-BODY ANTENNA LOCATIONS

In this study, seven on-body antennas are used to provide full coverage over the whole intestinal tract. The on-body antennas are located on the voxel-model's abdomen area, as shown in Fig. 4c. Previous studies presented in [25] and [26] have been carried out with five on-body antennas, which also provided sufficient coverage over the intestinal tract. However, now the number of on-body antennas is increased to seven to further improve coverage in the upper and lower parts of the gastrointestinal tract (GI) and stomach area. Additionally, the increased number of antennas can also facilitate the localization of the capsule, which is another area of interest.

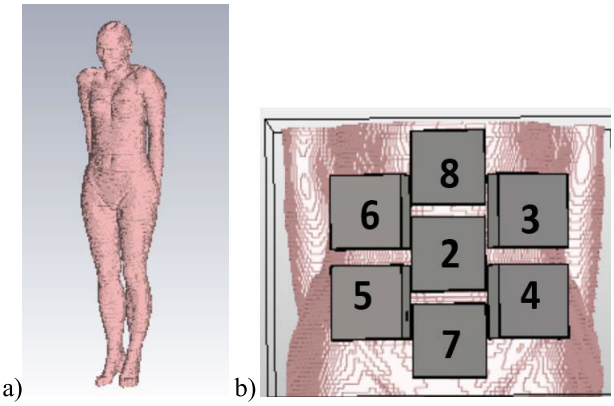

FIGURE 4. a) Laura-voxel model, b) On-body antenna locations on Laura.

The on-body antenna numbering is set according to the antenna port numbering of the simulation model: the port number 1 is the antenna port of the capsule antenna, and port numbers 2-8 for the on-body antennas. The on-body antenna - skin distance is approximately 4 mm, which corresponds to the thickness of a thin cloth. Due to the pixelation of the voxel models, size of the antenna and shape of the voxel model, the antenna-skin distance may slightly differ in some antenna locations which may have an impact on the propagation depth as discussed in [18].

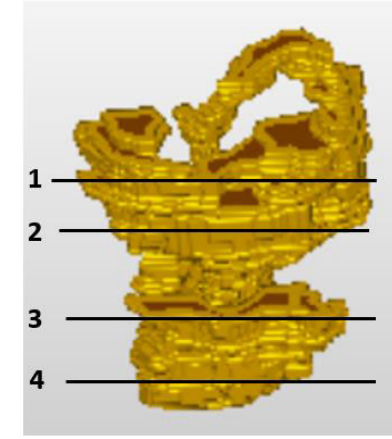

FIGURE 5. The cross-section levels in the small intestine.

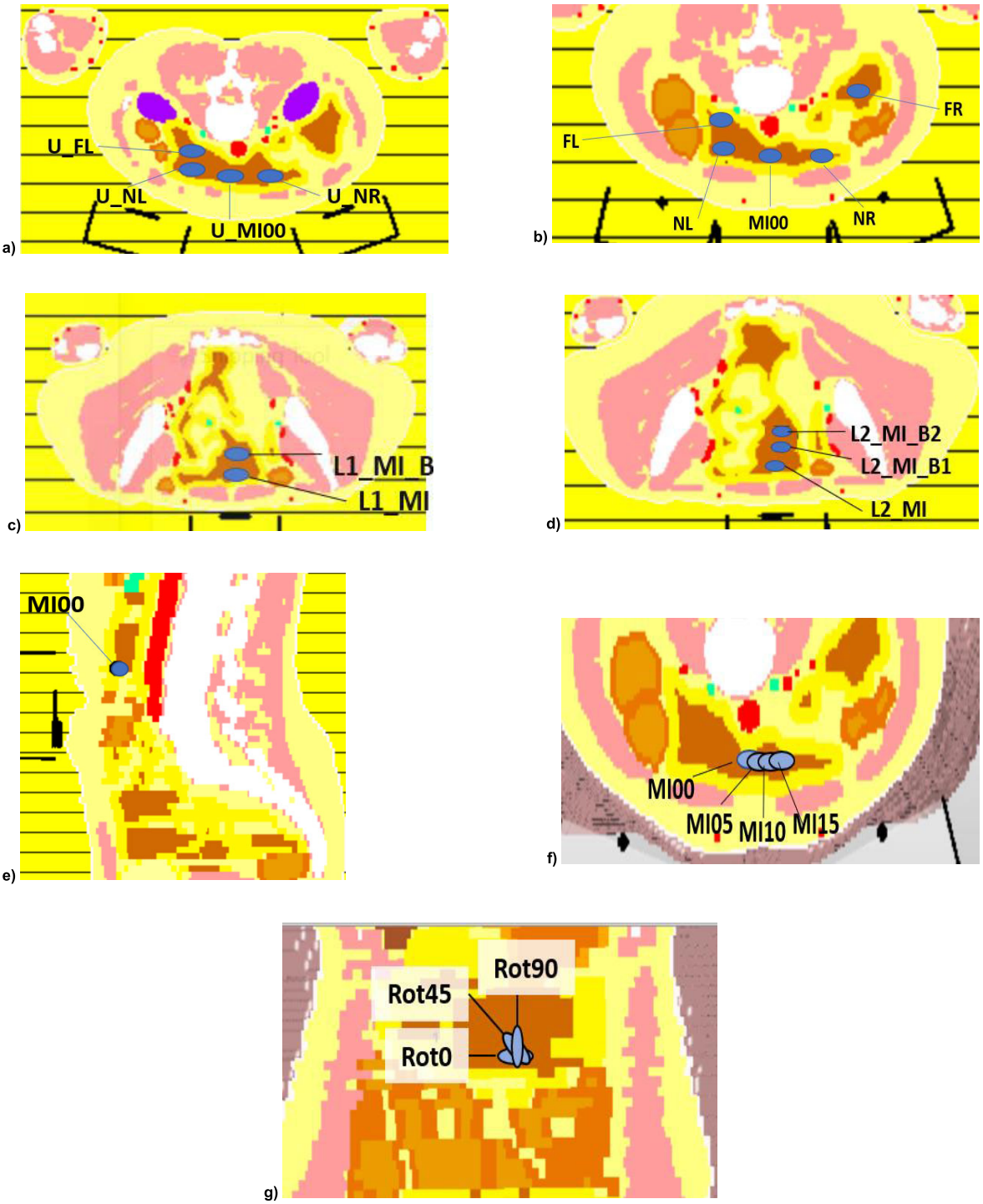

FIGURE 6. a-d) Evaluated capsule locations in small intestine at cross-section levels 1-4, e) vertical cross-section with capsule location MI00, f) capsule locations with small shifts, g) capsule rotations in MI10.

2) CAPSULE LOCATIONS IN SMALL INTESTINE AREA

Fig. 5 presents the four cross-section lines (1-4) in the voxel model's small intestine area in which the channel evaluations are carried out. Fig. 6a-d. present the cross-sections of Laura voxel model at these cross-section lines. Several different capsule locations are evaluated within each cross-section to understand channel variation inside the intestinal area more comprehensively. Cross-section line 2 is evaluated most in detail since it is among the widest region in the voxel's small intestinal area enabling channel evaluations in diverse channel conditions: ''near middle (MI00)'', ''near left (NL)'', ''near right (NR)'', ''far left (FL)'', and ''far right (FR)''

cases. Additionally, the impact of the capsule's small shift is evaluated by transferring the capsule from the location MI00 towards right 15 mm in the steps of 5 mm, as shown in Fig. 6e. Moreover, the impact of the capsule's rotation is studied by rotating capsule 45 and 90 degrees (Rot45 and Rot90) and evaluating channel characteristics in few selected locations of the gastrointestinal tract. Fig. 6 illustrates capsule rotations in MI10.

3) CAPSULE LOCATIONS IN COLON AREA

The first voxel-model based capsule channel evaluations throughout the colon area have already been presented by M. Särestöniemi et al in [26] with 5-antenna setup. The results presented in this paper are the extension for the previously presented results by including channel evaluations with 7 on-body antennas as well as including new locations in the sigmoid colon area. Fig. 7a presents all the evaluated locations in the colon area and Fig. 7b presents the cross-section for the location G0-G2 which has not been presented in [26].

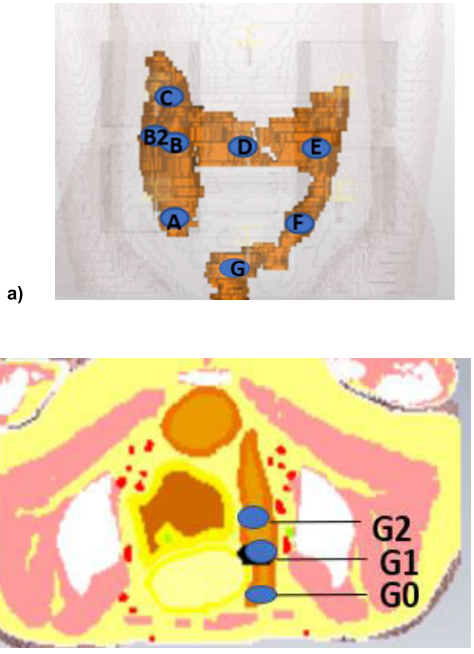

FIGURE 7. a) Evaluated capsule locations in colon area, b) cross-section in sigmoid colon area with locations G0, G1, and G2.

4) CAPSULE LOCATIONS IN STOMACH

This paper also evaluates whether the proposed 7-on-body antenna setup provides sufficient communication channel for the capsule in the stomach area as well. Fig. 8a presents the capsule location STO1, which is in the bottom of the stomach area, from the front view also showing the capsule position respect to the on-body antennas. Fig. 8b presents the cross-section of the voxel model in the level where the capsule is located. Besides, the channel characteristics are also evaluated in STO0, which is in the upper part of the stomach.

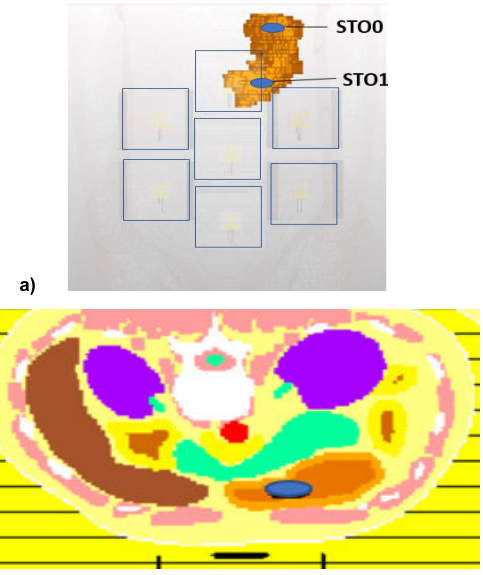

FIGURE 8. Evaluated capsule locations in the stomach area: a) front-view presenting the capsule locations in the stomach respected to the on-body antennas, b) the cross-section of the voxel model in capsule location STO1 case.

C. SIMULATION PARAMETERS AND COMPUTATIONAL RESOURCES

Our simulations were conducted within a frequency range of 0.5 to 5 GHz, using 1001 equally spaced frequency samples from which frequency band 3.75-4.25 GHz is extracted. We utilized a large number of mesh cells, approximately 333,000,000, to model the torso of Laura-voxel, on-body antennas, and the capsule model. To handle such a large number of mesh cells, we employed parallel processing on several cluster nodes, consisting of Intel Xeon E5-2640 v4 CPUs. Despite efficient parallel processing, the simulation time for the implant model varied between 1 and 6 days, depending on the computational load on the server computers.

To ensure accurate results, we set the boundary conditions for the model to "open" for the z-axis direction, which extends the touching geometry virtually to infinity, and "Open add space" for the x- and y-axis directions. This added some extra space with a determined distance to enable proper functionality of the antennas. For the remaining simulation parameters, we used the default settings provided by the simulator, which were appropriate for our simulations. The excitation signal, a pure sinusoid signal, was fed to the transmitter (Tx) antenna (the capsule antenna), i.e., to the Port 1. The simulator calculated and provided frequency domain results, such as the reflection coefficients for Tx and Rx antennas (S11, S22, S33,..., S88) and reverse and forward channel gains between different antennas S21, S12, S31, S13,..., S81 (i.e., frequency responses).

This study includes radio channel analysis both in frequency and time domains. Time domain conversion was carried out by performing an inverse discrete Fourier transform (IDFT) on the frequency domain channel parameters, which is explained in more detail in Section V.

III. PROPAGATION INSIDE THE ABDOMINAL TISSUES

In this section, we provide insight into how the signal propagates from the capsule antennas inside a GI track, through different tissues towards the on-body antenna by visualizing power flow in different capsule locations. The propagation prediction inside a human body is challenging due to several reasons. The dielectric properties of different tissues vary remarkably, leading to variations in propagation loss and propagation time. Additionally, reflections and refractions occur at the borders of different tissues. Furthermore, the complex and non-symmetric shapes of different tissues, as well as the huge variation of body constitutions of different people, pose challenges in channel modeling.

A. DIELECTRIC PROPERTIES IN TISSUES

Dielectric properties of different tissues depend mostly on the water-content [22]. For instance, muscle tissue contains about 75% water, whereas fat tissue only 10%. The relative permittivity and conductivity values of different abdominal tissues are presented in Table 1. As it can be seen, dielectric properties of fat tissue vary significantly from the other tissues: its relative permittivity at 4 GHz is only 5.18 whereas for muscle, small intestine, and large intestine it is slightly over 50. Relative permittivity for stomach is higher: 59. However, there is large variation in conductivities. The impact of relative permittivity for the propagating signal is that higher is its value, slower is the speed of propagating electromagnetic signal in that media. In general, the radio signal propagation speed inside a human body is slower than in free space [21], [22].

In this paper, we calculate propagation time for different in-body propagation paths from the capsule towards different on-body antennas utilizing information of the wavelength in different abdominal tissues. The wavelength in different tissues can be calculated using the equation [30]

$$\lambda_t = \frac{\lambda_0}{\sqrt{\varepsilon}_r \mathrm{Re}\left[\sqrt{1 - j\sigma/\omega\varepsilon_0\varepsilon_r}\right]} \quad (1)$$

where λ_t and λ_0 are wavelengths in the tissue and free space, correspondingly, ε_0 and ε_r are permittivity in a vacuum and relative permittivity of the tissue, σ is conductivity of the tissue, which also depends on the media and frequency, and ω is angular frequency.

TABLE 1. Dielectric properties of abdominal tissues at 4 GHz.

Tissue	Relative permittivity	Conductivity
Small intestine	51.6	4.62
Large intestine	51.3	3.46
Stomach	59.6	3.85
Muscle	50.8	3.02
Fat	5.12	0.18
Skin	36.6	2.34

TABLE 2. Wavelength in meters at 3.75, 4 and 4.25 GHz.

Tissue	3.75	4	4.25
Small intestine	0.0109	0.0102	0.0097
Large intestine	0.011	0.0103	0.0098
Stomach	0.0102	0.0096	0.0091
Muscle	0.011	0.0104	0.0098
Fat	0.0351	0.033	0.0311
Skin	0.0131	0.0122	0.01158

Table 2 presents the wavelength in meters in the tissues at the start, middle, and end frequencies of the frequency range of interest.

As can be seen, the wavelength in the tissues varies significantly, leading to differences in the propagation velocities. For example, the wavelength in the fat tissue is significantly different from that of other tissues, leading to a much higher propagation speed in fat tissue than in the muscle layer. Furthermore, power loss in fat tissue is significantly lower than in other tissues due to lower relative permittivity. Fat as a propagation medium has been studied actively, e.g., in [33], [35], and [36].

B. S11 EVALUATIONS IN DIFFERENT CAPSULE LOCATIONS

This subsection investigates how much capsule location effects on the reflection coefficient S11. Fig. 9 presents S11 in small intestine in two locations (MI10 and FR), colon (CE), and stomach (STO1). Additionally, S11 results with different rotation angles in MI10 are evaluated. As it can be seen, there is some variation between the simulated S11 in different capsule locations and rotations. However, the differences are relatively small: maximum 1 dB was noted between S11_STO1 S11_MI10_Rot90 cases. The S11 differences simulated in colon and small intestine areas are minor, only 0.75dB. These slightly varying differences in S11 are due to the changes in dielectric properties: since the dielectric properties of small intestine and colon are almost the same as seen in Table 1,

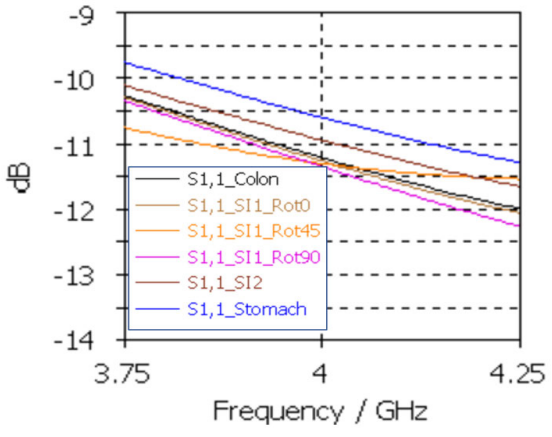

FIGURE 9. S11 parameters for capsule antenna at different capsule locations in the gastrointestinal track and rotation angles.

also the differences in S11s are minor. Instead, the relative permittivity of stomach is clearly higher than those of small intestine and colon, which yields to weaker S11 in stomach area.

The impact of the rotation affects also slightly on the S11, in this case maximum 0.7 dB. The differences are due to the changes of the vicinity of the intestine wall between different rotation cases since the tissue interfaces cause reflections towards the antenna. The closer and the larger the intestinal wall surface to the capsule, the weaker is the S11. The impact is naturally location-specific since the intestinal structure is complex and thus the S11 results for different rotation cases are specific for this certain location.

It is important to note that S11 primarily affects the efficiency of the antenna in radiating power to the medium, which in turn leads to reduced received power, while S21 is more directly related to the attenuation of the medium and the geometry of the transmission path. Changes in antenna matching can have an impact on both parameters and, in turn, on the overall channel attenuation. However, since the observed differences in S11 results are minor, further detailed analysis of its impact is left for future work.

C. POWER FLOW EVALUATIONS

In this section, in-body propagation from the capsule antenna at 4 GHz is studied using the notion of power flow. The average power flow density $\mathbf{S}_{av}$ is related to the complex Poynting vector as

$$Sav = \frac{1}{2}Re\,(\boldsymbol{S}) = \frac{1}{2}\mathrm{Re}(\mathbf{ExH}*), \tag{2}$$

in which $\mathbf{E}$ and $\mathbf{H}$ are the electric and magnetic field intensity [21]. The Poynting vector represents the directional energy flux (the energy transfer per unit area per unit time) of an electromagnetic field. The flux of the Poynting Vector through a certain surface represents the total electromagnetic power flowing through it.

Here we use arrow- based power flow representation which illustrates well how the signal components diffracts in different tissue borders and propagate towards different directions depending on the tissue type. The densification of the power flow arrows visualizes well the propagation paths, which are calculated in Section VI. Here, the power flow values (expressed as decibels) have been normalized so that 0 dB is the maximum, i.e., the value at the transmitting antenna, and the plotted dB range is from 0 dB to -80 dB. The values of the power flow are calculated along the propagation paths in Points A to D. Point A describes how much power has decreased as the signal has passed the intestinal area in the selected cross-section. Point B shows the power flow value inside the tissue in the vicinity of the closest antenna. Point C and D define the power flow values inside the fat layer in the vicinity of the next antennas along the selected cross-section. It is emphasized that presented power flow values are instant values in the selected points in the selected cross-sections.

Fig. 10a-d presents power flow illustrations at 4 GHz in different capsule locations in the small intestine (Fig. 10a-c) and colon (Fig. 10d-e), both closer to skin surface and deepest part of the intestine. Firstly, the capsule location MI00 is studied. The power flow for this location is studied earlier [19] but the illustration is repeated here to ease comparison between the ''near skin surface'' and ''deeper from skin surface'' cases. Fig. 10a shows how the capsule radiates to all the directions, but the radiation is strongest from the longer sides of the capsule. Fat as a propagation channel is obvious since it can easily reach even the back of the voxel from MI00. Besides, the power flow illustration shows how the signal can propagate deep inside the body through the visceral fat layers. Additionally, the vertical cross-section plot shown in Fig. 10b visualizes how the signal may propagate long distances through the outer fat layers, also reaching the antennas which are further from the capsule.

The densification of the power flow arrows in Fig. 10a shows three clear propagation paths towards the closest antennas: the first main path is the direct and shortest path from the capsule through the small intestine and fat layer towards the on-body antenna 2. Additionally, there are two paths from the capsule towards the antenna 3 and 6, mainly propagating through the fat layer. The values of the power flow are calculated along these paths in Points A to D, which are presented in Table 3. In Point A, power flow value is -40 dB which shows relatively modest power loss since the signal does not have to travel long distances inside the small intestine. The power flow in Point B is also at a relative high level since in this location, the signal is summed up from the multipath components coming from different directions. Besides, the multipath components arriving directly from the Point A need to travel only through the fat tissue in which the propagation loss is moderate. Point C and D define the power flow values inside the fat layer in the vicinity of the next antennas along the selected cross-section. The value in Point C is higher than in Point D since between A and D there is a wider muscle area in which propagation loss is higher due to higher ε_r of muscle compared to fat. Propagation times for these paths are shown in Section VI.

Next, we study power flow from the location FL in Fig. 10c, which illustrates how signals propagate from the locations which are deep inside the small intestine. As it can be noted, power flow from FL is much more narrowly distributed than in the case of MI00 due to the high propagation loss in the intestinal tissues. In this case, the value in Point A

TABLE 3. Normalized Power flow values in decibels at 4 GHz in the selected points in different capsule location cases.

Point	MI00	FL	C_B	C_B2
A	-40	-55	-36	-68
B	-49	-83	-49	-71
C	-64	-85	-58	-87
D	-68	-105	-83	-98

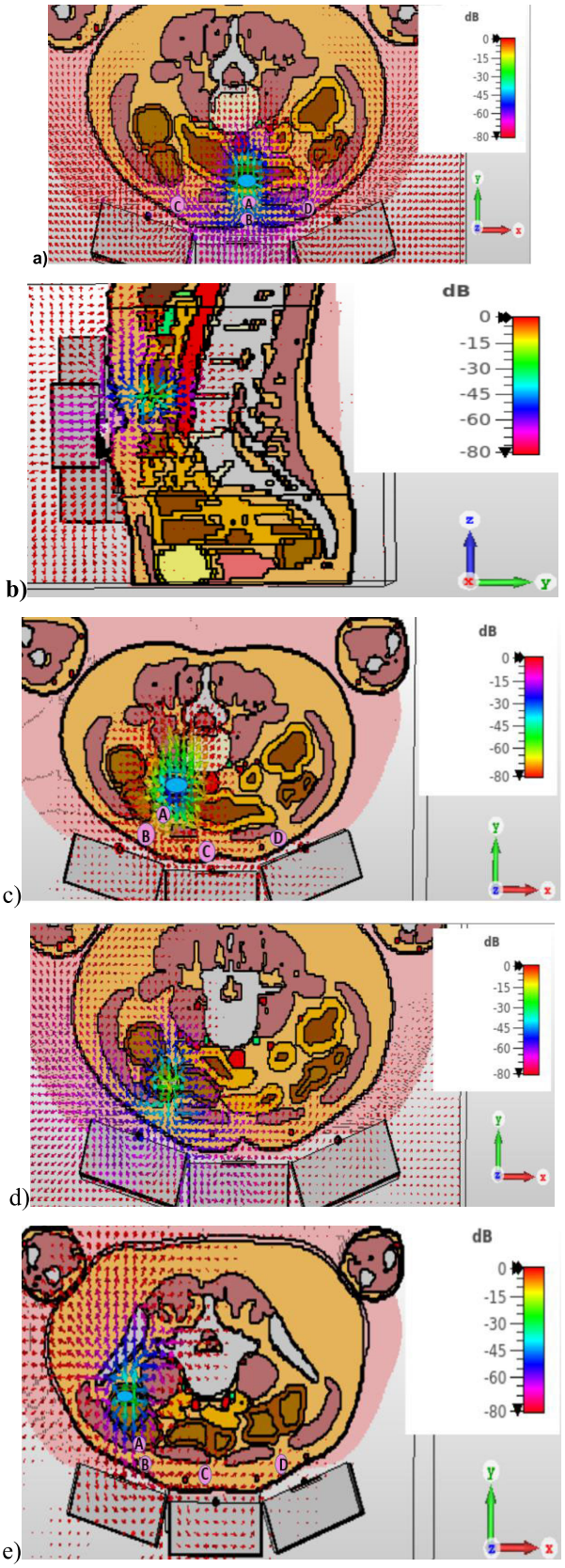

FIGURE 10. Power flow illustrations at 4 GHz to study signal propagation from the capsule towards on-body antennas, a) MI00, b) MI00, vertical cross-section, c) FL, d) colon B, e) colon B2.

is -55 dB which is 15 dB lower than in the case of MI00. Besides, power flow value in Point B is significantly lower in FL than in MI00, only -83 dB. Even the difference between the Points A and B is conspicuous in the case of FL, 28 dB whereas in the case of MI00 it was only 9 dB. The reason for this difference is the significantly narrower power distribution in the case of FL since the power flow value in location B is the 3D sum of all the multipath components.

Similar tendency can be found in the Colon locations C_B and C_B2. Power flow value in the location B is significantly lower in the case of C_B2, that is deeper inside the colon tissue, than in the location C_B. However, the power flow value in the point B for the case C_B2 is clearly higher than for the case FL.

IV. CHANNEL EVALUATIONS

In this section, the frequency and time domain channel characteristics between the capsule and the multiple on-body antennas are evaluated in 26 different capsule locations through the Laura voxel's gastrointestinal track from stomach to sigmoid colon. The aim is to visualize channel strength variation for different receiving antennas and reflect the results for antenna radiation patterns presented in Fig. 1a. Since this paper consists of the channel study results conducted in 26 different locations, only the most interesting cases are selected to be shown under few study categories. Table 4 summarizes all the simulated S-parameters at 3.75 GHz, 4 GHz, and 4.25 GHz, which are the start, center, and end frequencies in WBAN implant communication frequency range. The purpose of presenting these three values for each location is to demonstrate channel attenuation variation within the frequency band, especially in certain capsule locations. Channel attenuation values are reflected with radiation patterns presented for start, center, and end frequencies of this band in Fig.1b-c.

The channel attenuations in different capsule locations are discussed regarding the possibility for capsule localization. For the successful capsule localization, it is essential to obtain at least 4 links with moderate attenuation. In the literature, different WBAN link budget calculations have been presented with criterias for channel attenuation and receiver's sensitivity [31], [32].

A. EXAMPLES OF CHANNEL RESPONSE VARIATIONS

1) STOMACH

Firstly, the channel characteristics are evaluated as the capsule has entered in the bottom of the stomach after swallowing. Fig. 11 presents the channel frequency response (CFR) between the capsule and all the on-body antennas. As expected, S31 and S81, i.e., the channels for the on-body antennas 3 and 8, are the strongest since they are the closest antennas from the capsule location. The channel attenuation is moderate, 50 – 60 dB within the studied frequency band. The next strongest channels are S21, S41, and S61 having channel attenuation at best 68 dB, 68 dB,

TABLE 4. Channel parameters at different capsule locations throughout the gastrointestinal tract.

	S21 3.75/4/4.25 GHz	S31 3.75/4/4.25 GHz	S41 3.75/4/4.25 GHz	S51 3.75/4/4.25 GHz	S61 3.75/4/4.25 GHz	S71 3.75/4/4.25 GHz	S81 3.75/4/4.25 GHz
MI	-36/-41/-40	-55/-55/-49	-62/-55/-65	-72/-60/-78	-58/-50/-48	-75/-65/-65	-58/-60/-60
NR	-45/-50/-58	-67/-55/-65	-67/-68/-75	-84/-85/-82	-76/-70/-72	-84/-83/-82	-73/-81/-69
FR	-90/-87/-88	-72/-79/-80	-94/-94/-95	-113/-112/-110	-102/-96/-96	-112/-112/-115	-98/-100/-92
NL	-52/-65/-60	-65/-57/-58	-81/-76/-83	-78/-91/-79	-64/-62/-72	-89/-85/-100	-63/-69/-72
FL	-72/-83/-96	-84/-76/-78	-97/-95/-98	-100/-95/-98	-75/-74/-78	-115/-106/102	-80/-91/-95
U_MI_260	-48/-55/-52	-75/-55/-57	-82/-61/-69	-75/-60/-75	-69/-55/-57	-85/-84/-82	-42/-45/-50
U_NR_260	-66/-62/-65	-59/-55/-57	-79/-80/-82	-95/-72/-77	-68/-60/-62	-93/-85/-82	-63/-57/-55
U_NL_260	-64/-63/-75	-75/-63/-64	-84/-76/-84	-76/-75/-80	-56/-54/-56	-100/-92/-90	-80/-62/-63
U_FL_260	-77/-77/-87	-86/-77/-78	-95/-80/-97	-87/-90/-92	-69/-72/-75	-118/-120/-125	-90/-75/-82
L1_MI	-88/-82/-92	-92/-97/-106	-87/-77/-92	-91/-73/-74	-90/-87/-97	-65/-63/-62	-102/-98/-103
L1_MI_B1	-90/-82/-92	-65/-63/-61	-83/-78/-89	-91/-74/-75	-89/-86/-95	-66/-62/-61	-101/-98/-102
L2_MI	-88/-72/-95	-100 /-90/-90	-80/-72/-75	-83/-95/-78	-88/-84/-92	-57/-55/-55	-103/-93/-95
L2_MI_B1	-116/-108/-117	-120/-120/-110	-92/-93/-102	-99/-95/-97	-104/-102/-114	-68/-68/-69	-130/-118/-126
L2_MI_B2	-110/-98/-111	-112/-120/-108	-92/-97/-109	-100/-95/-98	-104/-105/-115	-75/-81/-102	-128/-122/-108
C_A	-75/-74/-71	-82/-80/-75	-83/-80/-76	-51/-58/-65	-81/-70/-85	-75/-70/-65	-100/-89/-89
C_B	-46/-45/-47	-64/-70/-56	-57/-58/-65	-54/-52/-57	-40/-45/-46	-76/-65/-64	-62/-61/-68
C_B2	-74/-65/-78	-81/-78-95	-76/-84/-88	-58/-67/-75	-74/-70/-80	-87/-85/-90	-96/-87/-85
C_C	-44/-45/-47	-62/-70/-55	-57/-59/-65	-53/-51/-59	-40/-45/-45	-90/-74/-75	-70/-68/-80
C_D	-40/-39/-39	-65/-62/-58	-54/-53/-55	-62/-52/-55	-68/-60/-59	-65/-61/-60	-60/-69/-57
C_E	-82/-52/-52	-67/-57/-67	-50/-54/-57	-80/-70/-65	-72/-70/-67	-64/-73/-65	-71/-73/-63
C_F	-73/-60/-57	-67/-65/-76	-50-47/-45	-81/-69/-70	-71/-73/-69	-53/-47/-45	-80/-77/-82
C_G0	-90/-85/-75	-90/-82/-82	-75/-75-75	-90/-72/-80	-84/-90/-91	-62/-65/-58	-100/-90/-90
C_G1	-102/-100/-102	-106/-100/-105	-96/-98/-99	-92/-90/-93	-110/-100/-100	-78/-75/-76	-110/105/-108
C_G2	-120/-125/-110	-122/-117/-120	-105/-105/-105	-110/-100/-110	-117/-120/-120	-102/-105/-100	-124/-102/-100
STO1	-71/-74/-69	-55/-52/-60	-72/-75/-78	-92/-80/-88	-66/-74/-85	-95/-78/-98	-58/-52/-49
STO0	-124/-125/-121	-112/-115/-125	-124/-121/--122	-132/-142/-142	-125/-135/-128	-135/-132/-140	-115/-111/-115

and 62 dB, respectively. However, at the frequency range 4 – 4.15 GHz, S61 drops significantly decreasing even below the S51 and S71, which are the furthest antennas in this capsule location. This phenomenon can be understood by studying the radiation patterns of the on-body antennas in Fig. 1 c-d. At 3.75 GHz, the lobe is stronger from antenna 6 towards the capsule location than at 4.25 GHz. The reason for relative high level of the channels for the furthest antennas 5 and 7, i.e., S51 and S71, at 4 GHz, is also understood from the radiation patterns. At 4 GHz, there is a strong lobe from the upper part of the on-body antenna towards the area where capsule is located. Instead at 4.25 GHz, the lobe is shifted, which can be seen in the decreased channel strengths. In this case, the channel attenuation is moderate for several on-body antennas and hence enabling reliable communication and capsule localization even with the receivers having lower sensitivity.

The capsule stays approximately 10-20 min in stomach. During that time, the activated capsule can take pictures around the stomach area with 3D camera if the capsule light is sufficient. The capsule can also take pictures while travelling through the esophagus and upper stomach. Next, the channel characteristics were evaluated between the capsule and the on-body antennas in the location STO0, which is on the upper part of the stomach. The channel parameters for STO0 case

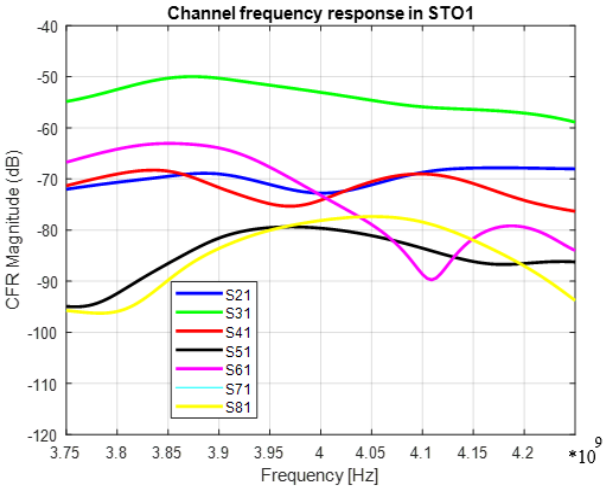

FIGURE 11. Frequency domain channel characteristics (S21,…, S81 parameters) between the capsule and each on-body antennas 2,…8) in the capsule location STO1 in the lower part of the stomach area.

can be found in Table 4. In this case, the channel attenuation is strong, between -110 to -140 dB within the frequency range of interest. Obviously, the distances to the closest on-body antennas 3 and 8 are excessive since S31 and S81 indicate weak channels as well. In addition to excessive distance to the

closest on-body antennas, another reason for strong channel attenuation is that the stomach is a thick organ with the upper part deeper inside the chest, and hence a fat tissue as a propagation medium cannot be exploited similarly as with locations STO1. Therefore, if the images are aimed to be sent instantaneously from each capsule location, one more on-body antenna would be needed on the upper chest area.

2) SMALL INTESTINE

a: CROSS-SECTION B

To better understand the channel characteristics in the small intestine, we evaluate the frequency and time domain channel characteristics between the capsule and multiple on-body antennas in cross-section level B. This cross-section is particularly noteworthy as it includes some of the widest regions in the voxel's small intestinal area enabling evaluations in very different locations in terms of propagation. As presented in Section II, this cross-section includes capsule locations near middle (MI), near left (NL), near right (NR), far left (FL), and far right (FR). Fig. 13a-e present the frequency domain channel characteristics, S21, …, S81, in MI00, NL, NR, FL, and FR locations, respectively, and Fig. 14a-e present the corresponding time domain channel characteristics.

In the case of MI00, which is a very centralized location with respect to the on-body antennas, the channel attenuation at different frequencies is modest for all the on-body antennas varying between 36 dB and 74 dB, as seen from the channel parameters in Fig. 12a. Channel attenuation for the antenna 2, which is the closest antenna to the capsule, is naturally smallest and smooth along the frequency range of interest, it is 36 dB – 42 dB. The next closest antennas, 3 and 6, are symmetrically located with respect to the capsule on its left and right sides but there is a clear difference in the channel attenuations. S31 and S61 values differ by even 4 dB at 4 GHz. This difference is due to the asymmetric radiation pattern of the on-body antenna towards the lower left and lower right directions, as seen in Figs. 2 b-c. The asymmetry between the right and left parts is clearest at 4 GHz. The on-body antenna 6 has stronger beam towards the capsule than the on-body antenna 3. This radiation pattern asymmetry is more pronounced between the upper left and upper right parts of the radiation patterns, which effects on the channels between the capsule and the on-body antennas 4 and 5. For instance, at 3.75 GHz, S51 is 10 dB larger than S41. In MI00's case, the 7-antenna setup will not bring significant improvement for capsule communications/ localization since the channels for the other on-body antennas are strong enough to provide a reliable communications link.

In the case of NL and NR, channel attenuations remain at a reasonable level for at least four closest antennas. In the case of NR, attenuations are smoother and milder than in NL. In NR, the attenuation variation between the four strongest channels is between 46 dB and 82 dB. Instead, with NL, variation between channel attenuations within the frequency range of interest is between 55 dB and 92 dB. However, there are deep fades in S21, S51, and S61, which cause attenuation drops up to 92 dB but otherwise the attenuations remain at a reasonable level. The deep drops in the case of NL can also be found in radiation patterns. Nevertheless, the notches occur at different frequencies and thus are less destructive.

The attenuation levels in the NL location are lower than in the NR location despite of being a similar distance from the on-body antennas. This difference can be attributed to the varying tissue compositions in these areas, as previously discussed in [33]. Specifically, there is a higher concentration of fat tissue and less muscle tissue in NL, which results in lower propagation loss and stronger channels compared to NR.

In terms of antenna setup, using seven on-body antennas provides a clear benefit for both NL and NR locations. Specifically, the seventh antenna is the third or fourth strongest channel in NL and the third or fifth strongest channel in NR, depending on the radiation pattern.

The FR and FL locations, located in the deepest parts of the small intestine, present a challenge due to high propagation loss. However, even the lowest attenuation levels of 70 dB or 78 dB, found in NL and NR respectively, are still manageable with receivers of higher sensitivity. However, successful capsule localization may be more difficult in these areas due to the stronger attenuation levels of the further antennas. Additionally, the inclusion of the seventh on-body antenna is beneficial in these areas as it is the third or fourth strongest channel.

Furthermore, the channel attenuation levels also vary greatly between FL and FR locations, with the channels in FR being weaker than in FL. This is primarily due to the greater distance between the capsule and the skin surface in FR, but is also influenced by the presence of a large visceral fat area in this location.

b: TIME DOMAIN EVALUATIONS

Human abdomen area including several different tissues with different dielectric properties is a multipath-rich propagation environment in in-body communications since the signal transmitted from the capsule experiences several diffractions and reflections when facing tissue borders. This could easily be seen in power flow illustrations presented in Fig. 10. Additionally, the use of cavities in the on-body antennas can ease capturing signals from wider areas.

To accurately capture the complex propagation characteristics of a multipath-rich environment, it is essential to perform time domain conversion from the channel transfer function or S21. This process involves transforming the frequency domain representation of the channel to the time domain, which is commonly done by the inverse discrete Fourier transform (IDFT), allowing for the visualization of the channel's impulse response. Additionally, polynomial interpolation-based oversampling technique is utilized to increase the number of samples per symbol period and therefore increases the resolution of the impulse response in the time domain. This

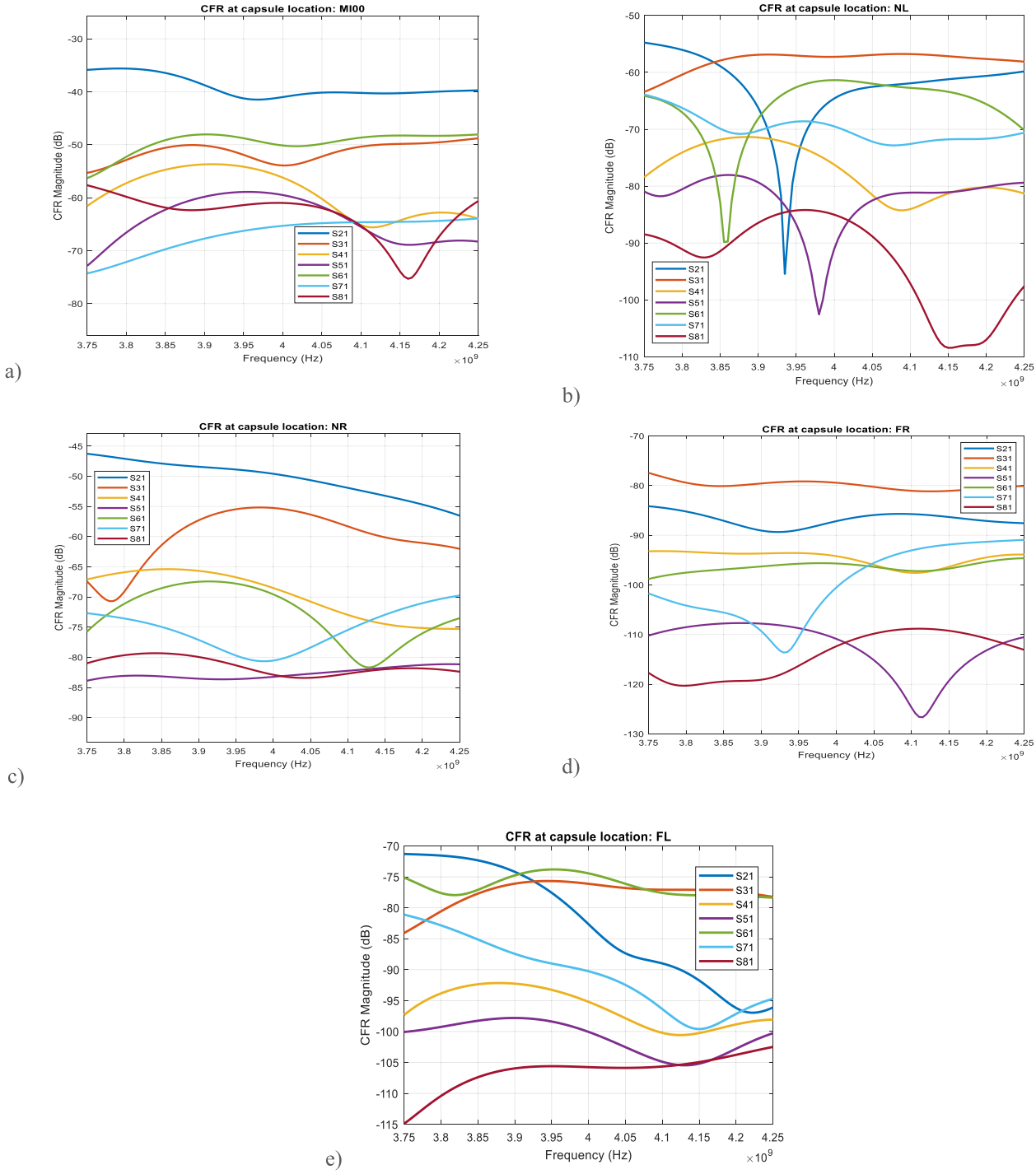

FIGURE 12. **Frequency domain channel characteristics (S21,...,S81) between the capsule and each on-body antennas 2,...8) in different locations of cross-section B: a) MI00, b) NL, c) NR, d) FL and e) FR.**

is achieved by taking multiple samples per symbol period, resulting in a higher resolution of the impulse response and a more accurate representation of the channel's behavior. In this study case, we use sampling interval 1/10.

These techniques are evident in the power delay profiles (PDP) of the IRs presented in Fig. 13a-e, where several strong multipath components arrive at the receiving on-body antennas within a time frame of just a few nanoseconds. In many cases, at least two IR peaks are at similar levels, as is the case with MI00 in Fig.13a. To maintain the clarity of the illustration, only the four strongest IRs are included in the figure. All of these strongest impulse responses have two almost equal strong peaks with a delay of 0.2 – 0.4 ns.

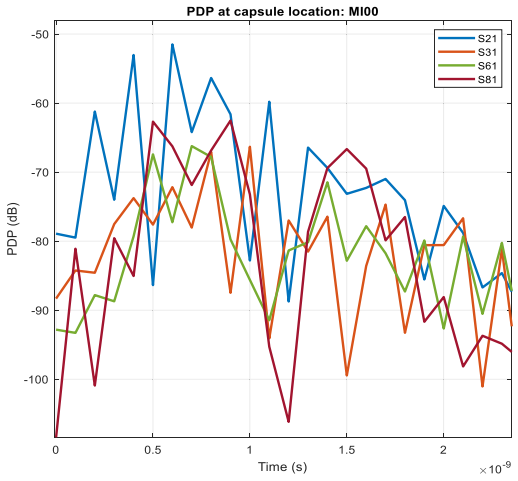

a)

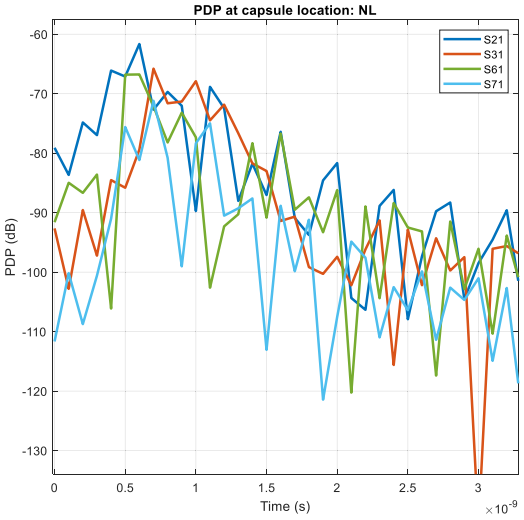

b)

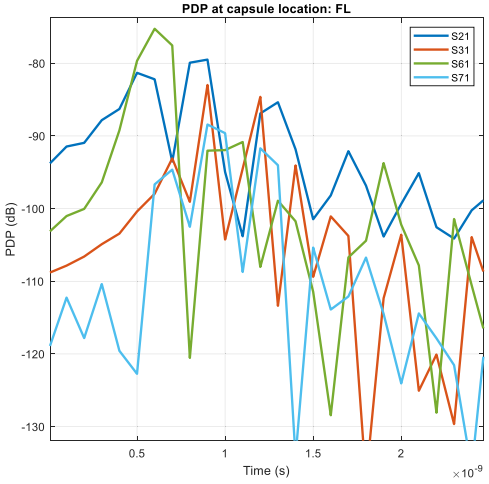

c)

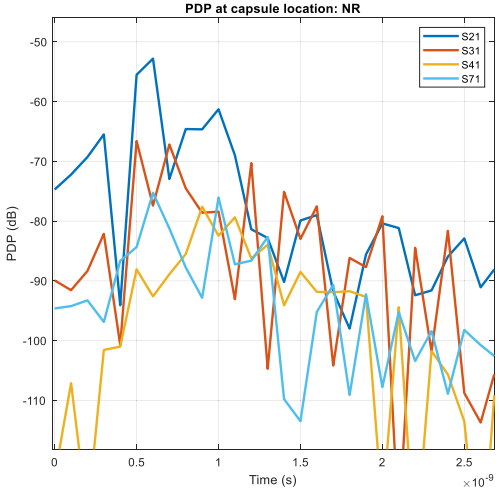

d)

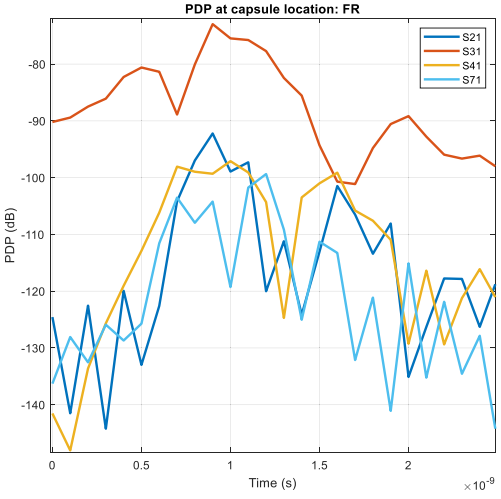

e)

FIGURE 13. Time domain channel characteristics (IR21, ..., IR81) in different locations of cross-section B: a) MI00, b) NL, c) NR, d) FL and e) FR.

Several strong multipath components arrive to the receiving on-body antennas during the time frame of few nanoseconds. In many cases, at least two of the IR peaks are at somewhat same level, as e.g. in the case of MI00 presented in Figs. 13a. In this case, only four strongest IRs are included in the figure due to clarity of the illustration. All these strongest impulse responses include two almost equal strong peaks with the delay of 0.2-0.4 ns.

Next, we conduct few propagation path calculations for the propagation paths expected from the power flow evaluations and verify the results with the time of arrival of the impulse response peaks. As discussed in [34], the propagation time t_d is calculated taking into the account the frequency f, the distance d that the signal travels through tissue, and the wavelength in the tissue λ as

$$t_d = \frac{d}{v} = \frac{d}{f\lambda} \tag{3}$$

Wavelengths on the different tissues were presented in Table 2. The propagation distance d is the thickness of the tissue layers on each propagation path, which is obtained from the coordinates of the voxel model.

First, the expected main paths are calculated in MI00 case. The expected main paths between the capsule and the on-body antenna 2 are illustrated in the vertical cross-section of the voxel model in Fig. 14a. Naturally, there are also numerous other multipath components which are summed in the receiving antennas. However, this section includes only few path descriptions for brevity.

The propagation distance in each of the tissues in each of the propagation paths is measured from the voxel model. The following notations are used for propagation distances in each tissue: d_s (thickness of the skin), d_{sm} (path length in small intestine tissue), d_f (path length in the fat tissue), d_m (path length in the muscle tissue).

Path IR21A is the shortest direct path from the capsule towards the skin layer through the small intestine and fat tissues. After propagation through the skin layer, signal enters the upper part of the antenna cavity region. The propagation distances travelled in different tissues are shown in Table 5. The propagation time, calculated based on Eq. (3), is 0.24 ns, which matches with the first peak of the IR21 in Fig. 13a.

Path IR21B is the most direct diagonal path from the capsule to the antenna center. In this case, the signal has to travel longer distances through the tissues, which effects on the propagation time 0.44 ns, which matches well with the time of the arrival of the IR peaks. As seen from power flow illustrations, the signal is a sum of multipath components travelling from a wider area.

Path IR21C is the indirect path propagation through visceral fat and out fat layers. Also in this case, the channel is a sum of several components arriving from different directions summing altogether at 0.62 ns. Since the propagation loss in the fat tissue is modest, the IR peaks are at high levels. The capsule antenna is omni-directional, it radiates different directions from the capsule. As seen from power flow

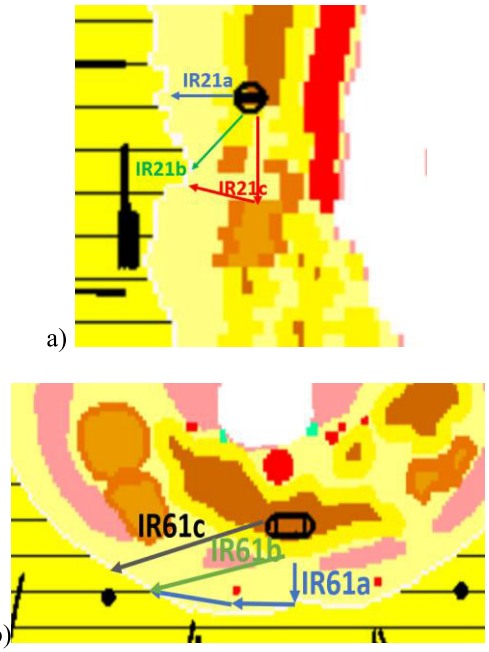

FIGURE 14. Propagation paths in MI00 case a) towards the on-body antenna 2 presented in vertical cross-section, b) towards the on-body antenna 6 presented in horizontal cross-section.

TABLE 5. Examples of the propagation paths in MI00.

Path	MI00			
	d_f (mm)	d_{sm} (mm)	d_{sm} (mm)	t_{tot} (ns)
Path21a	20	2	2	0.24
Path21b	29	5	2	0.44
Path21c	60	5	2	0.62
Path61a	43	5	2	0.49
Path61b	63	5	2	0.64
Path61c	70	30	2	1.32
Path81a	90	5	2	0.8
Path81b	67	5	2	0.67
Path81c	43	5	2	0.48

illustrations, part of those signals gradually diffracts towards the body surface and hence arrive slightly later than the PathIR21B. Received signal is a sum of different multipath components from different directions and thus strong peaks can be seen also at 0.8 ns and 1.2 ns

Path_IR61A Next, the propagation paths from the capsule towards antenna 6 is analyzed. In this case, the propagation paths are more easily visualized in horizontal cross-section presented in Fig. 14a. Besides of distances in horizontal cross-section, the vertical distance needs to be taken into account since the capsule is located 3.2 cm below the center point of the antenna 6. Path_IR61A is the clearest visible path from capsule to the on-body antenna 6 from the power flow illustration. It is the shortest distance from the capsule to the bottom of the skin tissue in which the signal diffracts

towards left and propagates through the fat tissue (towards left upwards) until reaching antenna 6 region. Corresponding peak in the impulse response is wide and covers several paths summing up at 0.64 ns.

Path_IR61B and **Path_IR61C** are the propagation paths on both sides of the left abdominal muscle, both well visible in the power flow illustrations. In the case of IR61B, the propagation time is 0.49 ns, which matches with the first peak of the impulse response as shown in Fig. 13a.

In Path_IR61C, the signal travels 3 cm in the small intestine before reaching the fat layer and continuing towards the capture area of antenna 6, yielding total propagation time 1.2 ns, which can also be noted as a peak in the impulse response. Obviously, there are also numerous other multipath components for instance through the muscle layer as well which yields higher propagation time.

Path_IR81s: The propagation from the capsule towards the on-body antenna 8 is similar to those of antenna 2, except now the signal travels a longer distance through the outer fat layer.

Path IR81A is the shortest direct path from the capsule towards the skin layer through the small intestine and fat tissues. After propagation facing the inner part of the skin tissue, the signal turns upwards and travels to the fat layer until reaching antenna 8. The propagation time will be 0.8 ns, which can also be seen as strong peak in the IR81 in Fig. 13a.

Path IR81B is the most direct diagonal path from the capsule to the antenna center yielding 0.67 ns. In the IR81, there is a wide peak visible from 0.49-0.7 ns. This peak includes all the signal components from the capsule travelling through outer fat and reaching the antenna 8 region. Since the antenna cavity is large, the antenna captures the signal from the wider area. As seen from power flow illustration, part of the signal travels inside the cavity towards the antenna center in the air. These signal components basically travel shorter distances inside the tissues than those reaching the antenna center level before propagating through skin tissue. Thus, there are signal components arriving at earlier time slot than those ones which are calculated with the propagation distance until the antenna center point. For instance, the vertical distance between the capsule and the lower cavity edge for the antenna 8 is 3 cm. If we repeat the calculations for PathIR81A and PathIR81B until the lower edge of the cavity for antenna 8, we obtain propagation times 0.63 ns (will be summed to Path61b) and 0.48 ns. The latter one is named as **PathIR81C** in Table 5.

The propagation path calculations for the on-body antenna 3 are similar than to on-body antenna 6. The only difference comes from the larger muscle area between the capsule and the on-body antenna, as discussed in the frequency domain results. The larger muscle area effects on the level and timing of the IR peaks. The on-body antennas with larger distance to the capsule will not be discussed here due to conciseness of the paper.

The impulse responses for NL, NR, FL, and FR cases are presented in Fig. 13b-e. Similar tendencies can be found also in these cases when we compare frequency and time domain channel evaluations, power flow illustrations, and propagation path calculations. Due to brevity, detailed reporting of these evaluations is left out from this paper.

c: CROSS-SECTION B

The results for cross-section B were closely examined due to its width, which allowed for evaluations under various channel conditions. Now, we will take a look at the upper portion of the small intestine, known as cross-section A. The capsule locations in this area are similar to those in MI00 and the channel attenuation values are studied from Table 4. It is worth noting that the channel attenuations for S21, …, S71 are only slightly larger than in cross-section B, as the signal travels smoothly through the outer fat layer towards the on-body antennas 2-7. The S81 values are at higher levels due to the shorter distance between the capsule and the antenna 8. The 7-on-body-antenna setup proves to be advantageous over the 5-on-body antenna setup as the channels for antenna 8 are the strongest.

d: CROSS-SECTION C AND D

In the next step, we will evaluate the channel characteristics in the lower part of the small intestine, in cross-sections C and D. The results are summarized in Table 4. In these cases, the on-body antenna 7 proves to be beneficial for capsule communications as S71 indicates the strongest channel for all evaluated points in cross-sections C and D. This is even true in the deepest location of the small intestine, L1_MI_B, L2_MI_B1, and L2_MI_B2 due to the larger amount of visceral fat in that area. The next strongest channels are S21, S41, and S51, with channel attenuation of only 72 dB at 4 GHz for S21.

3) COLON

Finally, the channel characteristics are evaluated through the colon area with 7-on-body antenna setup as well as including new results in the sigmoid colon area. Table 4 presents the results for 7-antenna-setup in the locations C_A, C_B, C_C, C_D, C_E, and C_F which were evaluated in [26]. As it is noted, the 7-antenna setup brings some benefits compared to the 5-antenna setup especially for the most challenging locations A and F.

Next, the channel characteristics are evaluated in the sigmoid colon area in the location G0, G1, and G2. The S21, … S81 values are presented in Table 4. As one can note, sigmoid colon is very channeling location due to large penetration depth requirements. The channel attenuation at G0 is still at resolvable level whereas location G1 requires a high-sensitive receiver. At the frequency range of interest, the channel attenuation in location G2 is excessive. For testing purposes, we located one more on-body antenna, antenna 9, at the lower back of the voxel model and conducted simulations in the capsule location G2. Fig. 15 presents the frequency domain channel characteristics between the capsule in the location G2 and the on-body antenna 9. For reference, S81values at the locations G2 and G0 are included. As one can note,

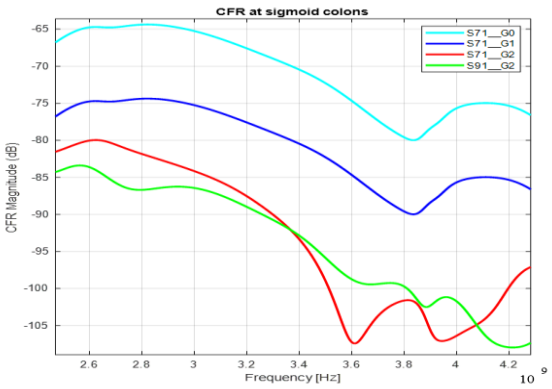

FIGURE 15. Frequency domain channel characteristics in sigmoid colon area at points G0, (front) G1 (middle), and G2 (back).

in the location G2 the S91 is at clearly higher level than the S81. S91 is almost at the same level as S81 in the capsule location G1. The reason for clearly higher propagation loss in the link between the capsule and on-body antenna 8 is the propagation environment; on the back area there is more visceral fat than on the front side. Therefore, the signal can propagate smoothly through the fat from the capsule to the antenna 9.

S21 parameters are presented for the wider frequency range in Fig. 15 in the purpose to show how at lower frequency range, i.e., at 1.5-2.5 GHz, the channel attenuation is moderate also in the capsule location G2; although that is out of the antennas' operational frequency range. Therefore, the use of lower frequencies in capsule endoscopy would be easier to ensure reliable communications. However, there is a strong interest in using UWB especially in studies targeting active capsule endoscopes due to several advantages the higher frequencies may provide (e.g., better throughput, improved resolution, and smaller size). Although lower frequencies can provide higher penetration depth underneath the skin, the physical dimensions of the antenna are then increasing leading to tradeoff between the usable frequency and size of the capsule.

B. IMPACT OF SMALL SHIFTS

In this subsection, the impact of the small capsule shifts is evaluated by transferring the capsule from the location MI00 in cross-section B with the steps of 5 mm towards right as shown in Fig. 6f. The channel frequency responses between the capsule and the closest antennas 2, 3, and 6 are presented in Fig. 16a-c, respectively. It is noted that even shift of 5 mm cause clear changes in the channel frequency responses: 4 - 5 dB in S21, 0 - 12 dB in S31, and 1 - 4 dB in S61 within the on-body antennas operational frequency range 3.75 - 4.25 GHz. The capsule shift of 15 mm may cause the difference up to 20 dB in S21, 9 dB in S31, and 25 dB in S61. The reason for such remarkable differences is due to the changes both in the propagation environment, i.e., the type and thickness of the tissues through which the multipath

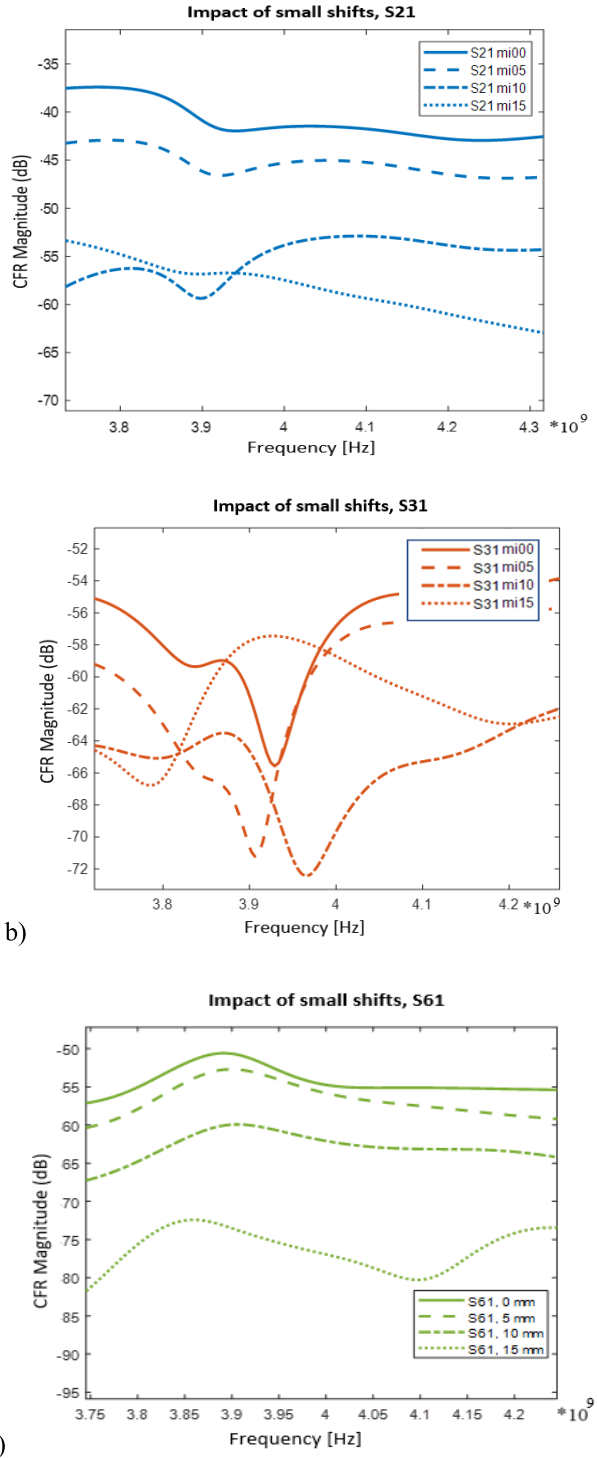

FIGURE 16. Impact of the capsule's small shifts on the channel attenuation for the three closest antennas: a) S21 b) S31 and S61 in the cross-section B.

components propagate, as well as in the antenna radiation patterns. As noted from Fig. 1b-d, the radiation pattern towards the body is highly fluctuating: strong beams vary with weaker or even null regions. Hence, even 5 mm changes in the capsule location can change drastically the channel strength. All the

TABLE 6. Impact of the capsule's small shifts.

	S21	S31	S41	S51	S61	S71	S81
MI00	-36/-41/-40	-55/-55/-49	-62/-55/-65	-72/-60/-78	-58/-50/-48	-75/-65/-65	-58/-60/-60
MI05	-37/-42/-42	-55/-57/-55	-66/-60/-68	-75/-70/-78	-54/-55/-57	-82/-72/-71	-73/-75/-63
MI10	-43/-46/-47	-60/-57/-56	-74/-64/-70	-80/-80/-90	-60/-57/-59	-92/-76/-74	-74/-76/-66
MI15	-57/-47/-54	-64/-70/-63	-68/-67/-74	-86/-96/-96	-67/-63/-65	-94/-81/-80	-75/-73/-76
MI20	-53/-57/-63	-65/-57/-63	-66/-75/-85	-76/-72/-75	-83/-77/-75	-86/-97/-92	-87/-99/-95

TABLE 7. Impact of the capsule's rotation on channel frequency responses.

	Rotation	S21	S31	S41	S51	S61	S71	S81
MI_10	0°	-43/-46/-47	-60/-57/-56	-74/-64/-70	-80/-80/-90	-60/-57/-59	-92/-76/-74	-74/-76/-66
	45°	-50/-51/-50	-60/-58/-57	-70/-65/-67	-79/-78/-75	-62/-62/-59	-86/-80/-81	-67/-65/-68
	90°	-48/-54/-57	-66/-69/-67	-66/-66/-73	-95/-80/-75	-69/-64/-67	-82/-87/-75	-72/-66/-72
L_MI_B1	0°	-89/-81/-71	-91/-98/-102	-89/-75/-90	-90/-72/-72	-90/-88/-95	-65/-64/-61	-102/-99/-104
	45°	-95/-90/-90	-95/-96/-92	-75/-77/-75	-86/-74/-76	-91/-93/-90	-55/-56/-56	-95/-98/-97
	90°	-85/-82/-82	-92/-95/-90	-72/-78/-73	-85/-75/-75	-108/-95/-92	-61/-60/-65	-94/-94/-110
L_MI_B2	0°	-110/-98/-111	-112/-120/-108	-92/-97/-109	-100/-95/-98	-104/-105/-115	-75/-81/-102	-128/-122/-108
	45°	-108/-108/-105	-108/-110/-109	-105/-98/-98	-110/-91/-99	-112/-105/-111	-78/-82/-85	-122/-118/-111
	90°	-99/-98/-105	-101/-113/-114	-88/-95/-100	-105/-90/-92	-102/-105/-105	-79/-78/-82	-102/-112/-110
C_A	0°	-75/-74/-71	-82/-80/-75	-83/-80/-76	-51/-58/-65	-81/-70/-85	-75/-70/-65	-99/-89/-89
	45°	-74/-78/-75	-92/-80/-75	-75/-72/-75	-51/-58/-61	-78/-68/-65	-85/-75/-65	-99/-81/-82
	90°	-80/-75/-90	-85/-80/-85	-80/-75/-82	-57/-52/-62	-76/-65/-66	-93/-85/-85	-70/-67/-65
NR	0°	-45/-50/-58	-67/-55/-65	-67/-68/-75	-84/-85/-82	-76/-70/-72	-84/-83/-82	-73/-81/-69
	45°	-50/-53/-60	-65/-50/-53	-72/-62/-70	-78/-72/-70	-65/60/-60	-98/-99/-105	-78/-78/-75
	90°	-42/-54/-60	-68/-58/-60	-66/-60/-68	-80/-70/-85	-80/-70/-60	-80/-85/-90	-79/-68/-65
FR	0°	-90/-87/-88	-72/-79/-80	-94/-94/-95	-113/-112/110	-102/-96/-96	-112/-112/115	-98/-100/-92
	45°	-85/-90/-90	-73/-70/-75	-92/-105/--93	-110/-130/-110	-100/-90/-91	-98/-93/-88	-112/-114/-110
	90°	-92/-95/-88	-88/-73/-78	-95/-95/-95	-112/-105/-115	-102/-105/-95	-98/-92/-88	-101/-100/-102
NL	0°	-52/-65/-60	-65/-57/-58	-81/-76/-83	-78/-91/-79	-64/-62/-72	-89/-85/-100	-63/-69/-72
	45°	-57/-58/ -63	-67/-60/-59	-81/-81/-86	-75/-77/-71	-69/ -63/-56	-94/ -85/ -90	-64/ -65/ -63
	90°	-55/-63/-63	-72/-73/-66	-77/-70/-81	-73/-80/-75	-60/-83/-60	-94/-80/-90	-72/-73/-66
FL	0°	-72/-83/-96	-84/-76/-78	-97/-95/-98	-100/-95/-98	-75/-74/-78	-115/-106/-99	-80/-91/-95
	45°	-63 /-66 /-75	-84/ -88/ -85	-93/ -101/ -102	-83/ -84/ -86	-84/ -72/ -72	-103/ -98/ -90	-86/ -83/ -79
	90°	-69/ -72/ -72	-84/ -102/ -88	-95/ -95/ -96	-75/ -71/ -74	-75 /-71/-74	-101 / 95/ -92	-94/ -83/ -78

channel parameters obtained when simulating the impact of small shifts are summarized in Table 6.

C. IMPACT OF CAPSULE ROTATION

The position of the capsule in the small intestine can be adjusted to various rotation angles. Since both the capsule antenna and the on-body antennas are linearly polarized, more channel attenuation is expected to occur when the capsule is rotated. A previous study on the impact of the capsule's rotation, using the Laura voxel model, was carried out for the first time in the MI00 case in [20]. This study showed a clear increase in channel attenuation as the capsule was rotated 90 degrees. Additionally, the study presented in [20] included investigations on the impact of rotation using a layered human tissue model for comparison. The results of the impact of rotation between the voxel model and the layered tissue model were found to be slightly different. In this paper, we will study the impact of rotation 45 and 90 degrees, ''Rot45'' and ''Rot90'', respectively, in various capsule locations, with a focus on two specific locations: MI10 and L_MI_B.

The frequency domain channel characteristics for the closest antennas in the locations MI10 (S21) and MI_B (S71) are presented in Figs. 17a-c, respectively. Table 6 summarizes the channel attenuations for all the antennas in these locations. As seen from Fig. 17a, the rotation can significantly dilute the channel in MI00 remarkably with a difference of 10 dB to 20 dB. From 3.75 – 3.95 GHz, the channel is weakest at ''Rot45'', whereas from 3.95 GHz onwards ''Rot90'' is the most attenuated. However, even in the worst case, the channel attenuation is modest enabling a reliable communications link. A similar tendency can be seen for S31 (in Table 6), with a maximum difference of 20 dB between the direct and non-rotated case. However, in this case the difference between the ''Rot0'' and ''Rot45'' case is only 0.2 dB at minimum.

The rotation study in capsule location L_MI_B is particularly interesting. In this case, the channel is less attenuated

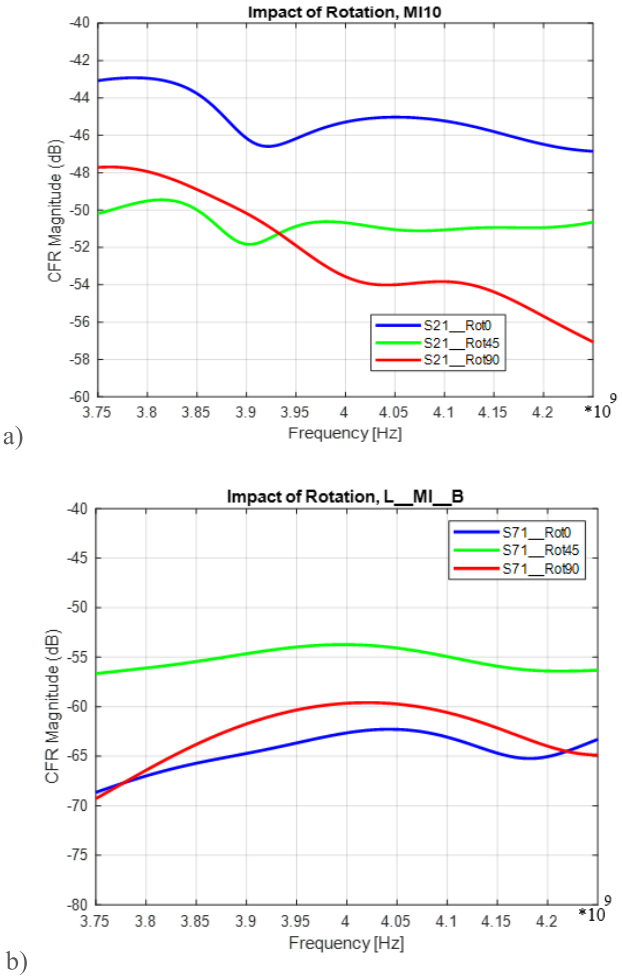

FIGURE 17. Impact of the capsule's rotation in channel parameters a) MII10 case in cross-section 2 and b) L1_MI_B case in cross-section 3.

in the rotated case than in the original case up to 4.13 GHz, after which "Rot90" experiences the strongest attenuation. The "Rot45" case remains less attenuated within the frequency range of interest. This is due to the capsule's most favorable orientation with respect to the on-body antenna's radiation pattern in this location. As seen from Fig. 18a, in this capsule location, the capsule is located in an area with some visible notches. In the case of "Rot 0", the notchy area affects the capsule more than in the cases of "Rot45" and "Rot90". For example, in "Rot45", the capsule is reaching an area with a stronger beam as shown in Fig. 18b, which presents a radiation pattern at 3.75 GHz. Additionally, in the case of "Rot90", the capsule orientation is more favorable for the on-body antenna's stronger beams. Furthermore, "Rot45" brings the capsule's radiating side closer to the edge between the small intestine and visceral fat. This naturally reduces the propagation loss, as the signal radiating from the capsule travels a slightly shorter distance in small intestine tissue than in fat tissue. More channel realization comparisons between the rotation cases can be found in Table 7.

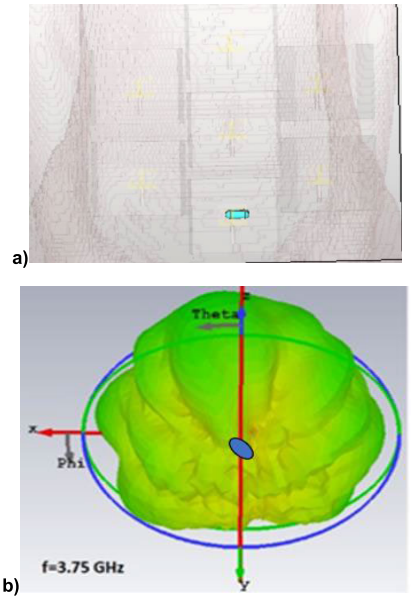

FIGURE 18. a) Capsule location L_MI_B respect to the on-body antennas, b) Capsule's location respect to the closest on-body antenna 7, illustrated with its radiation pattern to show notches in different rotation cases.

V. PATH LOSS EVALUATION

Path loss represents the reduction in transmitted power as a signal travels through different depths of the medium. For an in-body environment, path loss in decibels can be derived from the simulated channel frequency response. We will then evaluate the overall path loss and determine which of the available path loss models would provide the best fit for our data.

In this section, we will evaluate the path loss between the capsule and the on-body antennas in various scenarios that best represent different propagation environments. We have chosen scenarios that provide the most comprehensive understanding of the effects of the capsule's location and orientation on path loss with respect to each of the on-body antennas, which can be used to roughly estimate the coverage of the on-body antennas.

A. EFFECTS OF THE CAPSULE'S LOCATION AND ORIENTATION ON PATH LOSS MEASUREMENTS

Path loss represents the reduction in transmitted power when signal propagates through different depths of the medium. For an in-body environment, path loss in decibels can be derived from the channel frequency response using

$$PL\,(\mathrm{dB}) = -10\log_{10}\left\{\sum_{i=1}^{N}\frac{\left|H\left(f_i\right)\right|^2}{N}\right\}, \qquad (4)$$

where $H(f_i)$ is the simulated complex channel frequency response at the i-th frequency bin, and N is the total number of the frequency bins.

The in-body path loss characteristics are influenced by many factors such as the type and thickness of the surrounding tissues, and when the capsule is rotated, the conditions

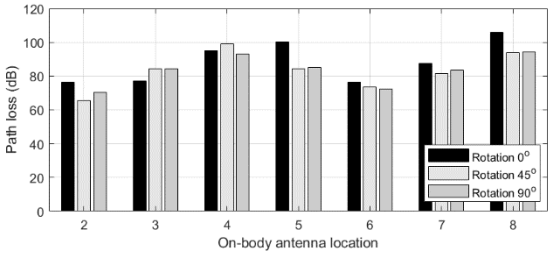

a) Capsule's location FL

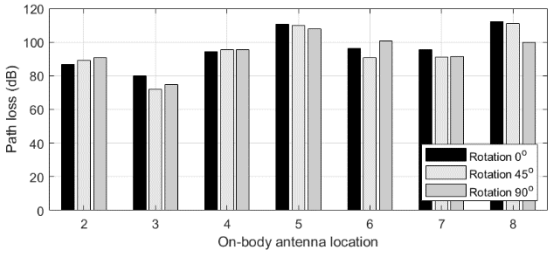

b) Capsule's location FR

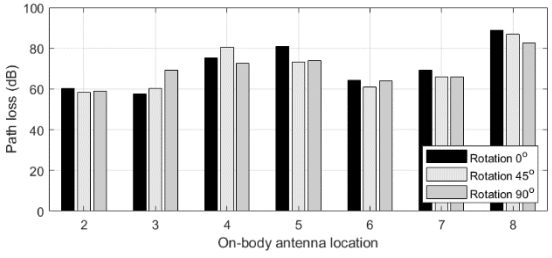

c) Capsule's location NL

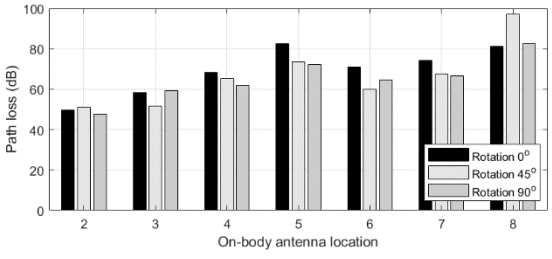

d) Capsule's location NR

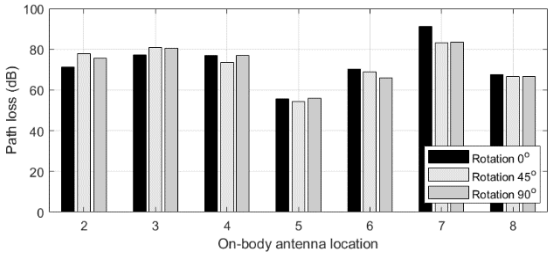

e) Capsule's location CA

FIGURE 19. Path loss results at capsule's locations FL, FR, NL, NR, and CA with capsule's rotations of 0, 45, and 90 degrees.

of the propagation paths change, resulting in changes in the observed path losses. The effects of the capsule's location and orientation on path loss results are plotted in Fig. 19a-e.

From Fig.19a-e, when we consider the overall path loss in every capsule's location, we can see that a group of two to three on-body antennas with the lower path loss values are the ones that are closest to the capsule. However, for the on-body

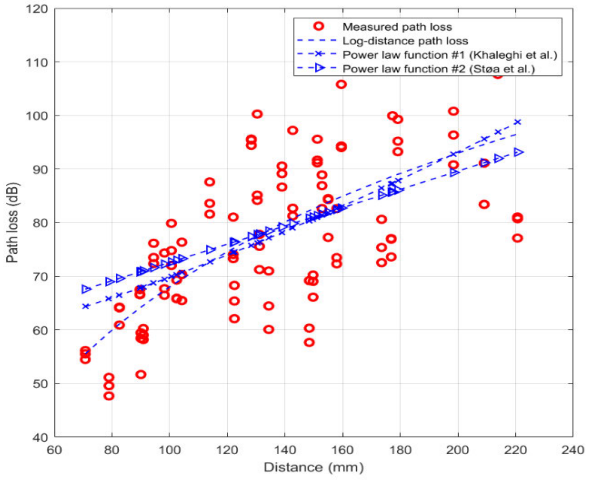

FIGURE 20. Path loss models fitting on the entire simulated channel frequency response.

antennas that are farther away from the capsule, this does not hold true due to the strong multipath effect.

In addition, we will also consider the effects of the capsule's rotation. We can see that in some cases, the changes in path loss are insignificant, for example around 0.1 dB at the capsule's location CA with the on-body antenna 8. However, in other capsule's locations, the changes can be quite significant, for example more than 10 dB difference at capsule's location NR with the on-body antenna 8. Fortunately, according to these plots, not all on-body antennas are susceptible to signal drop due to capsule's rotation at the same time. Therefore, techniques such as antenna diversity can be used to stabilize data transmission.

Lastly, we will investigate the importance of on-body antenna placement. We can see that for most of the capsule's locations, the on-body antennas in the center and the upper region of the abdomen, i.e., antenna 2, 3, and in some cases 4 and 6 provide a good coverage for the capsule's data transmission. However, for the capsule's location CA, the on-body antennas on the lower part of the abdomen, i.e., antennas 5 and 8 are more effective.

B. PATH LOSS MODEL

By using all of the selected simulated path losses obtained from all capsule's locations and orientations, we evaluate the overall path loss, and see how the commonly used path loss models for the in-body propagation channel perform with our data.

Generally, the log-distance model is used to describe the propagation channel in free-space setting. The model is be described as

$$\boldsymbol{PL}\,(\mathbf{dB}) = PL_{\mathbf{0}}(\mathrm{dB}) + \mathbf{10}\boldsymbol{n}\,\mathbf{log}_{10}\frac{\boldsymbol{d}}{\boldsymbol{d_0}}, \tag{5}$$

where $PL_{\mathbf{0}}$ is the path loss at the reference distance $\boldsymbol{d_0}$, $\boldsymbol{d}$ is the distance between the capsule and the on-body receiving antenna, which are calculated from the on- body antenna and capsule coordinates from Tables 8 and 9, respectively.

TABLE 8. On-body antennas' coordinates.

Antenna Location	Coordinates (mm)		
	x	y	z
2	12.85	-113.43	202.50
3	110.74	-94.06	252.50
4	110.74	-94.06	147.50
5	-84.11	-97.68	147.50
6	-84.11	-97.68	252.50
7	12.85	-109.43	302.50
8	12.85	-97.43	102.50

TABLE 9. Capsule coordinates.

Capsule Location	Coordinates (mm)		
	x	y	z
FL	-26.75	-24.00	238.47
FR	86.60	1.00	230.20
NL	-26.75	-40.00	238.47
NR	37.90	-45.00	232.80
CA	-55.10	-40.80	117.10

Besides, $\boldsymbol{n}$ is the path loss exponent. However, the authors in [17] showed that the model also works well with their in-body channel measurements. Other path loss models are also available. For example, authors in [11] suggested that an empirical exponential power law function as described in Eq. 5 would provide a better fit

$$\boldsymbol{PL}\,(\mathbf{dB}) = PL_{\boldsymbol{0}}(\mathrm{dB}) + a\left(\frac{\boldsymbol{d}}{\boldsymbol{d_0}}\right)^{\boldsymbol{m}}, \tag{6}$$

where $\boldsymbol{a}$ is the fitting constant, and $\boldsymbol{m}$ is the path loss exponent. Note that $\boldsymbol{n}$ and $\boldsymbol{m}$ in Eq. (5) and (6) are both called path loss exponents, but they are indeed two different values. Another path loss model proposed by [9] is the linear power law function, which is described as

$$\boldsymbol{PL}\,(\mathbf{dB}) = PL_{\boldsymbol{0}}(\mathrm{dB}) + \boldsymbol{k}\left(\frac{\boldsymbol{d}}{\boldsymbol{d_0}}\right), \tag{7}$$

where $\boldsymbol{k}$ is the gradient fitting constant.

We consider all these three potential path loss models to see how they match with our simulation results. By using the channel frequency response simulation results obtained from all the selected in-body capsule's locations and rotations using all seven on-body antennas, the overall path loss fitting and the corresponding root mean square error (RMSE) are displayed in Fig.20 and Table 10, respectively.

Based on our simulations, all three path loss models offer a comparable performance in terms of the RMSE values. The log-distance model has the lowest RMSE, followed by the exponential and linear power law function, respectively. As a result, the log-distance path loss performs slightly better than the other models for our data, with the path loss exponent $\boldsymbol{n} = \mathbf{8.30}$.

VI. SUMMARY AND CONCLUSION

This paper delves into a thorough examination of radio channel characteristics between a capsule endoscope and a 7-on-body antenna setup throughout the gastrointestinal tract in the WBAN implant frequency range of 3.75 – 4.25 GHz. An anatomically realistic human voxel model was utilized in the evaluations, and the channel characteristics were evaluated between the capsule and the on-body antennas in various parts of the stomach, small intestine, and colon, resulting in 363 different channel realizations, including studies on the impact of the capsule rotation in certain locations. The study includes analysis of frequency and time domain channel characteristics, reflecting the results with power flow representations, and propagation path calculations. The study was carried out using cavity-backed directional antennas to enhance the communications link, even when the capsule is deep inside the tissues.

TABLE 10. RMSE of the path loss model fitting.

Path loss model	RMSE (dB)
Log-distance	10.73
Exponential power law function	11.32
Linear power law function	11.58

The presented results indicate that the channel attenuation remains at a resolvable level in most cases, even deep inside the tissues. For the localization of the capsule, it is recommended to have at least four resolvable communications links, which is met in most cases, especially if high-sensitive receivers can be used. The most challenging location is the sigmoid colon location G2, in which the simulated channel attenuation is over 100 dB for all the antennas in the frequency range of interest, due to the challenging propagation environment and high propagation loss in the tissues. However, locating one on-body antenna on the lower back significantly improves the channel strength, especially if the receivers have higher sensitivity. It was also noted that at a lower frequency range (1 – 2 GHz), the channel attenuation would not be excessive, although the range is out of the antennas' operational frequency range. Thus, the use of lower frequencies in capsule endoscopy could make it easier to ensure reliable communications, even in the deepest locations. Nevertheless, there has been increased interest in using UWB in studies targeting active capsule endoscopes, due to the advantages that higher frequencies may provide (throughput, resolution, size, etc.).

In general, cavity-backed antennas are considered to have excessive size for practical solutions, as the size of the cavity depends on the frequency. However, there are studies on realizing cavity-backed antennas with smaller dimensions. The presented comparison between the propagation path calculations, power flow illustrations, and channel characteristics offers insight into how the signal propagates inside the abdominal tissues from the capsule. The deep knowledge of antennas' behavior on the human body is crucial, as the antenna radiation pattern has a significant impact on the channel characterization. The next step is to consider the use of flexible or textile antennas, which could be unobtrusively

embedded inside a cloth, allowing for the placement of antennas on both front and back sides of the body.

The investigations in this paper are restricted only for a simple omni-direction capsule antenna model. Recently, there has published several capsule antennas with optimized features for different frequency ranges. The use of more optimized antennas in the capsule could improve slightly the S1 parameter. As a future work, we will evaluate the impact the of different capsule antennas and their characteristics on the channel parameters at different capsule locations.

In the near future, our aim is also to carry out measurements using realistic shaped intestinal phantoms presented in [37] and compare the simulation and measurement results. We will investigate opportunities to use other voxel models with different body constitutions in the simulations. In [18], we have shown that CST's over-weighted voxel models Donna and Hugo have some shortcomings and restrictions for multiantenna capsule endoscopy investigations and thus, other human voxel models need to be considered. Moreover, we will also study capsule localization utilizing the comprehensive data set presented in this paper.

ACKNOWLEDGMENT

Dr. Chaimaa Kissi and Dr. Marko Sonkki are acknowledged for their contribution on on-body antenna design. Dr. Markus Berg is acknowledged for capsule antenna design. Prof. Carlos Pomalaza-Raez, who sadly passed away, in March 2022, has had a significant contribution in our research in fields of in-body propagation and capsule endoscopy communications.

REFERENCES

[1] B. Akpunonu, J. Hummell, J. D. Akpunonu, and S. Ud Din, "Capsule endoscopy in gastrointestinal disease: Evaluation, diagnosis, and treatment," *Cleveland Clinic J. Med.*, vol. 89, no. 4, pp. 200–211, Apr. 2022.

[2] S. H. Kim and H. J. Chun, "Capsule endoscopy: Pitfalls and approaches to overcome," *Diagnostics*, vol. 11, no. 10, p. 1765, Sep. 2021, doi: 10.3390/diagnostics11101765.

[3] D. R. Cave, S. Hakimian, and K. Patel, "Current controversies concerning capsule endoscopy," *Digestive Diseases Sci.*, vol. 64, no. 11, pp. 3040–3047, Nov. 2019.

[4] J. Flemming and S. Cameron, "Small bowel capsule endoscopy: Indications, results, and clinical benefit in a university environment," *Medicine*, vol. 97, no. 14, p. e0148, 2018.

[5] S. Alzahrani, H. Al Doghaither, and A. Al'Ghafari, "General insight into cancer: An overview of colorectal cancer (review)," *Mol. Clin. Oncol.*, vol. 15, no. 6, pp. 1–8, Nov. 2021, doi: 10.3892/mco.2021.2433.

[6] B. González-Suárez, I. K. Araujo, C. Romero, C. R. de Miguel, J. R. Ayuso, A. Pozo, M. Vila-Casadesus, A. Serradesanferm, A. Gines, G. Fernandez-Esparrach, and M. Pellise, "Colon capsule endoscopy versus CT colonography in FIT-positive colorectal cancer screening subjects: A prospective randomised trial—The VICOCA study," *BMC Med.*, vol. 18, no. 1, pp. 1–11, Dec. 2020, doi: 10.1186/s12916-020-01717-4.

[7] M. S. Ismail, G. Murphy, S. Semenov, and D. McNamara, "Comparing colon capsule endoscopy to colonoscopy; A symptomatic patient's perspective," *BMC Gastroenterol.*, vol. 22, no. 1, p. 31, Dec. 2022, doi: 10.1186/s12876-021-02081-0.

[8] O. Bchir, M. M. B. Ismail, and N. AlZahrani, "Multiple bleeding detection in wireless capsule endoscopy," *Signal, Image Video Process.*, vol. 13, no. 1, pp. 121–126, Feb. 2019.

[9] S. Stoa, R. Chavez-Santiago, and I. Balasingham, "An ultra wideband communication channel model for the human abdominal region," in *Proc. IEEE Globecom Workshops*, Dec. 2010, pp. 246–250, doi: 10.1109/GLOCOMW.2010.5700319.

[10] S. Støa, R. Chavez-Santiago, and I. Balasingham, "An ultra wideband communication channel model for capsule endoscopy," in *Proc. 3rd Int. Symp. Appl. Sci. Biomed. Commun. Technol. (ISABEL)*, Rome, Italy, 2010, pp. 1–5, doi: 10.1109/ISABEL.2010.5702854.

[11] A. Khaleghi, R. Chavez-Santiago, X. Liang, I. Balasingham, V. C. M. Leung, and T. A. Ramstad, "On ultra wideband channel modeling for in-body communications," in *Proc. IEEE 5th Int. Symp. Wireless Pervasive Comput.*, May 2010, pp. 140–145, doi: 10.1109/ISWPC.2010.5483804.

[12] A. F. Demir, Q. H. Abbasi, Z. E. Ankarali, A. Alomainy, K. Qaraqe, E. Serpedin, and H. Arslan, "Anatomical region-specific in vivo wireless communication channel characterization," *IEEE J. Biomed. Health Informat.*, vol. 21, no. 5, pp. 1254–1262, Sep. 2017.

[13] K. M. S. Thotahewa, J.-M. Redouté, and M. R. Yuce, "Propagation, power absorption, and temperature analysis of UWB wireless capsule endoscopy devices operating in the human body," *IEEE Trans. Microw. Theory Techn.*, vol. 63, no. 11, pp. 3823–3833, Nov. 2015, doi: 10.1109/TMTT.2015.2482492.

[14] M. Barbi, C. Garcia-Pardo, A. Nevarez, V. P. Beltran, and N. Cardona, "UWB RSS-based localization for capsule endoscopy using a multilayer phantom and in vivo measurements," *IEEE Trans. Antennas Propag.*, vol. 67, no. 8, pp. 5035–5043, Aug. 2019, doi: 10.1109/TAP.2019.2916629.

[15] J.-C. Brumm, H. Strohm, and G. Bauch, "A stochastic channel model for ultra wideband in-body communication," in *Proc. 41st Annu. Int. Conf. IEEE Eng. Med. Biol. Soc. (EMBC)*, Jul. 2019, pp. 4032–4035.

[16] J. Li, Z. Nie, Y. Liu, L. Wang, and Y. Hao, "Characterization of in-body radio channels for wireless implants," *IEEE Sensors J.*, vol. 17, no. 5, pp. 1528–1537, Mar. 2017.

[17] C. Garcia-Pardo, M. Barbi, S. Perez-Simbor, and N. Cardona, "UWB channel characterization for wireless capsule endoscopy localization," in *Proc. IEEE Int. Conf. Commun. Workshops (ICC Workshops)*, Jun. 2020, pp. 1–6, doi: 10.1109/ICCWorkshops49005.2020.9145270.

[18] M. Särestöniemi, C. Pomalaza-Ráez, C., Kissi, M. Berg, M. Hämäläinen, and J. Iinatti, "WBAN channel characteristics between capsule endoscope and receiving directive UWB on-body antennas," *IEEE Access*, vol. 8, pp. 55953–55968, 2020.

[19] M. Särestöniemi, C. Pomalaza-Ráez, C., Kissi, M. Berg, M. Hämäläinen, and J. Iinatti, "In-body power distribution for abdominal monitoring and implant communications systems," in *Proc. 16th Int. Symp. Wireless Commun. Syst.*, Sep. 2019, pp. 457–462.

[20] M. Särestöniemi, C. Pomalaza-Ráez, C., Kissi, M. Berg, M. Hämäläinen, and J. Iinatti, "UWB-WBAN radio channel characteristics between the endoscope capsule and on-body antenna," in *Body Area Networks: Smart IoT and Big Data for Intelligent Health Management*. Cham, Switzerland: Springer, 2019.

[21] S. J. Orfanidis. (2002). *Electromagnetic Waves and Antennas*. [Online]. Available: http://www.ece.rutgers.edu/~orfanidi/ewa/

[22] (2022). *IT IS Foundation*. Accessed: Jan. 8, 2022. [Online]. Available: https://www.itis.ethz.ch/virtual-population/tissue-properties/databaseM

[23] H. Zhang, X. Chen, M. Li, F. Yang, and S. Xu, "A compact dual-band folded-cavity antenna for microwave biomedical imaging applications," in *Proc. IEEE Int. Conf. Comput. Electromagn. (ICCEM)*, Shanghai, China, Mar. 2019, pp. 1–3, doi: 10.1109/COMPEM.2019.8779102.

[24] C. Kissi, M. Särestöniemi, C. Pomalaza-Raez, M. Sonkki, and M. N. Srifi, "Low-UWB directive antenna for wireless capsule endoscopy localization," in *Proc. 13th EAI Int. Conf. Body Area Netw. (BODYNETS)*, in Springer Innovations in Communication and Computing, C. Sugimoto, H. Farhadi, and M. Hämäläinen, Eds. Cham, Switzerland: Springer, Mar. 2018, pp. 1–9, doi: 10.1007/978-3-030-29897-5_38.

[25] M. Sarestoniemi, C. P. Raez, C. Kissi, and J. Iinatti, "Propagation study of UWB capsule endoscope with multiple on-body antennas," in *Proc. 15th Int. Symp. Med. Inf. Commun. Technol. (ISMICT)*, Xiamen, China, Apr. 2021, pp. 215–220, doi: 10.1109/ISMICT51748.2021.9434909.

[26] M. Sarestoniemi, C. Pomalaza-Raez, and J. Iinatti, "Radio channel study for colon capsule endoscopy with low-band UWB multiple antenna system," in *Proc. IEEE 16th Int. Symp. Med. Inf. Commun. Technol. (ISMICT)*, Lincoln, NE, USA, May 2022, pp. 1–6, doi: 10.1109/ISMICT56646.2022.9828189.

[27] H. Mateen, R. Basar, A. U. Ahmed, and M. Y. Ahmad, "Localization of wireless capsule endoscope: A systematic review," *IEEE Sensors J.*, vol. 17, no. 5, pp. 1197–1206, Mar. 2017, doi: 10.1109/JSEN.2016.2645945.

[28] *CST Microwave Studio*. Accessed: Jan. 21, 2022. [Online]. Available: http://www.cst.com
[29] *IEEE Standard for Local and Metropolitan Area Networks—Part 15.6: Wireless Body Area Networks*, IEEE Standard 802.15.6-2012, pp. 1–271, 2012.
[30] J. Wang and Q. Wang, *Body Area Communications: Channel Modeling, Communication Systems, and EMC*. Hoboken, NJ, USA: Wiley, 2012.
[31] O. R. Sparrow, R. Vauche, N. Dehaese, S. Bourdel, J. Gaubert, I. B. Amor, E. Muhr, P. Losco, and O. Fourquin, "High rate UWB CMOS transceiver chipset for WBAN and biomedical applications," *Analog Integr. Circuits Process.*, vol. 81, no. 1, pp. 215–227, 2014.
[32] J. O. Ha, S. H. Jung, M. C. Park, K. H. Lee, and Y. S. Eo, "A fully integrated 3–5 GHz UWB RF transceiver for WBAN applications," in *IEEE MTT-S Int. Microw. Symp. Dig.*, 2013, pp. 1–3.
[33] M. Sarestoniemi, C. Pomalaza-Raez, C. Kissi, and J. Iinatti, "Simulation and measurement data-based study on fat as propagation medium in WBAN abdominal implant communication systems," *IEEE Access*, vol. 9, pp. 46240–46259, 2021.
[34] M. SarestoNiemi, C. Pomalaza-raez, Z. Bi, T. Kumpuniemi, C. Kissi, M. Sonkki, M. Hamalainen, and J. Iinattit, "Comprehensive study on the impact of sternotomy wires on UWB WBAN channel characteristics on the human chest area," *IEEE Access*, vol. 7, pp. 74670–74682, 2019, doi: 10.1109/ACCESS.2019.2920067.
[35] N. B. Asan, D. Noreland, E. Hassan, S. R. M. Shah, A. Rydberg, T. J. Blokhuis, P. O. Carlsson, T. Voigt, and R. Augustine, "Intra-body microwave communication through adipose tissue," *Healthcare Technol. Lett.*, vol. 4, no. 4, pp. 115–121, 2017.
[36] N. B. Asan, E. Hassan, J. Velander, S. R. M. Shah, D. Noreland, T. J. Blokhuis, E. Wadbro, M. Berggren, T. Voigt, and R. Augustine, "Characterization of the fat channel for intra-body communication at R-band frequencies," *Sensors*, vol. 18, no. 9, p. 2752, 2018.
[37] M. Sarestoniemi, R. Dessai, C. Heredia, J. Hakala, S. Myllymaki, and T. Myllyla, "Novel realistic 3D phantom emulation platforms for human torso and head at microwave range," Univ. Oulu, Oulu, Finland, Tech. Rep. 08032023, Apr. 2023.

MARIELLA SÄRESTÖNIEMI (Senior Member, IEEE) received the M.Sc., Lic.Tech., and Dr. (Tech.) degrees from the University of Oulu, Finland, in 2003, 2005, and 2020, respectively. She is currently an Adjunct Professor and a Researcher with the Centre for Wireless Communications, a research unit, Faculty of Information Technology and Electrical Engineering, and the Research Unit of Health Sciences and Technology, Faculty of Medicine, University of Oulu. Her research interests include medical ICT, wireless body area networks, BAN channel modeling, realistic simulation, and emulation platform development, including human tissue phantom development and detection of abnormalities in the tissues using multimodal techniques.

ATTAPHONGSE TAPARUGSSANAGORN received the B.Eng. degree from Chulalongkorn University, Thailand, in 1997, the M.Sc. degree in electrical engineering from Technische Universität Kaiserslautern, Germany, in 2001, and the Dr.Tech. degree from the University of Oulu, Finland, in 2007. Right after his undergraduate study, he was an Engineer with the Telecommunications Transmission Department, Siemens Ltd., Bangkok, for two years. He gained experience as a Researcher with the Institute of Communications, University of Stuttgart, after his master's study, until 2003. After that, he joined the Centre for Wireless Communications (CWC), University of Oulu, in 2003, until he received the Dr. (Tech.) degree. In 2008, he continued with CWC as a Postdoctoral Researcher and was with Yokohama National University, Yokohama, Japan, as a Visiting Postdoctoral Researcher. After he returned home to Thailand, in 2011, he joined the Asian Institute of Technology (AIT) as an Adjunct Faculty. In 2012, he joined the National Electronics and Computer Technology Center (NECTEC) as a full-time employee. Since August 2015, he has been a full-time Faculty Member with AIT. He is currently an Associate Professor with the Department of ICT. His research interests include signal processing, statistical signal processing (detection and estimation techniques), wireless communications engineering, information theory, the Internet of Things, and machine/deep learning for various applications.

JUTHATIP WISANMONGKOL received the B.Eng. and M.Eng. degrees from Kasetsart University, Thailand, in 2006 and 2015, respectively, and the D.Eng. degree from the Asian Institute of Technology, Thailand, in 2022. She is currently an Assistant Researcher with the Location and Automatic Identification System Research Team, National Electronics and Computer Technology Center (NECTEC), Thailand. Her research interests include wireless localization and signal processing.

MATTI HÄMÄLÄINEN (Senior Member, IEEE) received the M.Sc., Lic.Tech., and Dr.Sc. degrees from the University of Oulu, Finland, in 1994, 2002, and 2006, respectively. He has been a fix-termed IAS Visiting Professor with Yokohama National University, Japan. He is currently an Adjunct Professor and a University Researcher with the Centre for Wireless Communications, University of Oulu. He has published more than 190 scientific publications. He is the co-editor of one book, coauthor of one book and two book chapters, and also holds one patent. His research interests include ultrawideband systems, radio channel modeling, wireless body area networks, and medical ICT. He is a member of the European Telecommunications Standard Institute (ETSI) Smart Body Area Network (SmartBAN) Group. He served as a reviewer for IEEE and IET journals and as a technical program committee member for numerous IEEE conferences. He was the General Chair of Bodynets 2018 and is the Steering Committee Co-Chair of the ISMICT Conference Series.

JARI IINATTI (Senior Member, IEEE) received the M.Sc., Lic.Tech., and Dr.Tech. degrees in electrical engineering from the University of Oulu, Oulu, Finland, in 1989, 1993, and 1997, respectively. From 1989 to 1997, he was a Research Scientist with the Telecommunication Laboratory, University of Oulu. From 1997 to 2002, he was acting as a Professor in digital transmission techniques and a Senior Research Scientist, the Project Manager, and the Research Director of the Center for Wireless Communications, University of Oulu. Since 2002, he has been a Professor of telecommunication theory. He is currently the Head of the Centre for Wireless Communications—Networks and Systems. He has authored about 250 international journal articles and conference papers, holds six patents, and is the co-editor of the book *UWB Theory and Applications* (Wiley & Sons Ltd., Chichester, U.K., 2004). He has supervised 19 doctoral theses and over 60 master's theses. His research interests include future wireless communications systems, transceiver algorithms, wireless body area networks (WBANs), and medical ICT. He has been a technical program committee (TPC) member in about 25 conferences. He was the TPC Co-Chair of the IEEE PIMRC2006, BodyNets2012, and PIMRC2014, the TPC Chair of the ISMICT2007, the General Co-Chair of the ISMICT2011, ISMICT2014, and ISMICT2015, and the TPC Program Track Co-Chair of BodyNets 2012. He was also an Organizer of the FEELIT 2008, the FEELIT2011, the UWBAN2012, and the UWBAN2013. He is also the Steering Committee Co-Chair of the ISMICT Series.